Pebbles and sands on asteroid (162173) Ryugu: On-site observation and returned particles from two landing sites

Authors: S. Tachibana*, H. Sawada, R. Okazaki, Y. Takano, K. Sakamoto, Y. N. Miura, C. Okamoto, H. Yano, S. Yamanouchi, P. Michell, Y. Zhang, S. Schwartz, F. Thuillet, H. Yurimoto, T. Nakamura, T. Noguchi, H. Yabuta, H. Naraoka, A. Tsuchiyama, N. Imae, K. Kurosawa, A. M. Nakamura, K. Ogawa, S. Sugita, T. Morota, R. Honda, S. Kameda, E. Tatsumi, Y. Cho, K. Yoshioka, Y. Yokota, M. Hayakawa, M. Matsuoka, N. Sakatani, M. Yamada, T. Kouyama, H. Suzuki, C. Honda, T. Yoshimitsu, T. Kubota, H. Demura, T. Yada, M. Nishimura, K. Yogata, A. Nakato, M. Yoshitake, A. Iwamae, S. Furuya, K. Hatakeda, A. Miyazaki, K. Kumagai, T. Okada , M. Abe, T. Usui, T. R. Ireland, M. Fujimoto, T. Yamada, M. Arakawa, H. C. Connolly, Jr. , A. Fujii, S. Hasegawa, N. Hirata, N. Hirata, C. Hirose, S. Hosoda, Y. Iijima, H. Ikeda, M. Ishiguro, Y. Ishihara, T. Iwata, S. Kikuchi, K. Kitazato, D. S. Lauretta, G. Libourel, B. Marty, K. Matsumoto, T. Michikami, Y. Mimasu, A. Miura, O. Mori, K. Nakamura-Messenger, N. Namiki, A. Nguyen, L. R. Nittler, H. Noda, R. Noguchi, N. Ogawa, G. Ono, M. Ozaki, H. Senshu, T. Shimada, Y. Shimaki, K. Shirai, S. Soldini, T. Takahashi, Y. Takei, H. Takeuchi, R. Tsukizaki, K. Wada, T. Yamaguchi, Y. Yamamoto, K. Yoshikawa, K. Yumoto, M. E. Zolensky, S. Nakazawa, F. Terui, S. Tanaka, T. Saiki, M. Yoshikawa, S. Watanabe, Y. Tsuda

Affiliations: *Not yet*

[1]Affiliations should be preceded by superscript numbers corresponding to the author list, and each affiliation should end with a period.

[2]Each affiliation should be a separate paragraph.

[3]You can include group authors, but please include a list of the actual authors in the Supplementary Materials.

*Correspondence to: tachi@eps.s.u-tokyo.ac.jp

†Additional author notes should be indicated with symbols (for example, for current addresses).

Abstract: The Hayabusa2 spacecraft made two successful landing operations onto the surface of C-type asteroid (162173) Ryugu to collect the asteroidal surface and sub-surface material. Close-up observation of the second touchdown site suggests that the impact ejecta from the artificial crater was present at the surface and should be part of the collected samples. Surface pebbles observed at two landing sites show morphological variations from elongated block to sub-equant block. Hayabusa2 delivered its reentry capsule enclosing the surface grains to the Earth on December 6, 2020. The color, shape, structure, and their variations of returned pebbles and sands, exceeding 5 grams in total, are consistent with those of Ryugu surface material, suggesting that the returned sample well represent the asteroid Ryugu.

One Sentence Summary: Hayabusa2 collected and returned more than 5 grams of Ryugu surface pebbles and sands that are well representative of the asteroid. (less than 150 characters)

Main Text:

Asteroids are small celestial bodies that are leftovers of the building blocks of planets. The spectroscopic similarity with carbonaceous meteorites indicates that asteroids belonging to the C taxonomic type, one of the main asteroid types, consist of carbonaceous chondrite-like materials containing hydrated silicates and organic matter. Such hydrated asteroids would have delivered water and organics to the proto-Earth. Samples from C-type asteroids are expected to contain the record of the Solar System evolution from its beginning (or even before) to current times (*1*). They should also record recent surface activities and processes as observed for particles from S-type asteroid (25143) Itokawa (*2–6*).

The Hayabusa2 spacecraft explored C-type near-Earth asteroid (162173) Ryugu from June 2018 to November 2019 to investigate the physical and compositional properties of the asteroid and to return surface samples to Earth. Hayabusa2 discovered that Ryugu is a top-shaped rubble-pile body (mean radius of 448 ± 2 m) (*7, 8*). Albite its ubiquitously dark colored nature, Ryugu surface shows a variety of reflectance spectra due to mixing of materials with bluish and reddish tints (*8, 9*) and the presence of some bright boulders related to S-type asteroids (*10*). The reddish color would have resulted from surface alteration of bluish materials occurring within the recent 10^6–10^7 years (*9*). A weak 2.72-μm absorption feature of O-H vibration in hydrous silicates was found over the surface (*11*). The 2.72-μm absorption is weaker than that of hydrated carbonaceous chondrites (*11*) and of B-type asteroid (101955) Bennu (*12–15*). This weakness could be due either to dehydration of originally hydrous silicates or weak aqueous alteration in the Ryugu's parent planetesimal (*8, 11*). In-situ observation by the MASCOT lander showed that the surface is not covered with fine regolith (*16*) like the rough terrain of Itokawa and that a ~3-cm pebble has a thermal inertia of ~280 J m^{-2} K^{-1} $s^{-1/2}$, which is much lower than the thermal inertia of chondrites, implying that the tensile strength of the pebble is only a few hundred kPa (*17*). Similar low thermal inertia (~300 J m^{-2} K^{-1} $s^{-1/2}$) was also obtained for many boulders (*18*). The artificial impact experiment by the Small Carry-on Impactor (SCI) suggests that Ryugu's surface is composed, at least partially, of a cohesionless material like loose sand (*19*). The infrared observation of the artificial crater found the spectral property similar to but slightly different from that of the surface (*20*). This spectral feature of sub-surface material (1 meter from the surface) indicates that the 2.72-μm absorption feature of Ryugu is primary, reflecting the process occurring on the Ryugu's parent planetesimal (*20*).

Hayabusa2 made its first landing (TD1) on February 22, 2019 (*9*), which was the first landing ever on a C-type asteroid, and the second landing (TD2) nearby the artificial crater on July 11, 2019 to collect surface samples and impact ejecta (sub-surface samples) (Fig. 1). The two landing locations looked similar, being covered with boulders and pebbles (Fig. 1). In both landing operations, a 5-gram tantalum projectile was successfully shot through the sampler horn (*1, 20–22*) at ~300 ± 30 m s^{-1} when the sampler horn touched the Ryugu surface.

A series of images of the sampler horn during the landing operations were taken by a small monitor camera (CAM-H) (Fig. 2 and movie S1) (*23*). One second after the projectile firing at TD1, about ten particles were identified beneath or nearby the sampler horn (Fig. 2c). The number of particles increased to ~20 in the next image, and there were three particles moving towards CAM-H (Fig. 2). The ejection angle and velocity of these particles are roughly estimated to be about 50–60° and 1–2 m s^{-1}, respectively (*23*). Their ejection angle was within the range measured in projectile-shooting experiments at the Earth's gravity (1-g) (40–60°; fig.

S1) (*23*) and consistent with the most frequent angle range (48–54°) in the Hayabusa2 sampling simulations (*24*). On these bases, we conclude that these particles correspond to ejecta produced by the projectile impact. The ejected particles identified nearby the rocket coupling ring were centimeter in size (Fig. 2). Centimeter-sized pebbles were found in the proximity images of the TD1 site (*9*) and at different surface locations observed by the lander MASCOT (*16, 17*) and the MINERVA-II-1B rover (Fig. 3). The MINERVA-II-1B rover also observed ejection of centimeter-sized particles associated with its hop on the surface (Fig. 3) (*23*). This suggests that centimeter-sized pebbles, which are not strongly adhered to larger cobbles and boulders, are present over the surface.

The total mass of the three ejecta particles in Fig. 2 is estimated to be in the range of 0.3–3 g, assuming spherical particles with a diameter of 0.5–1 cm and the bulk density of ~2 g cm^{-3}. If all the ejecta particles in Fig. 2 (~20 in number) have the same ejection velocity as the three particles moving towards CAM-H, the total amount of ejecta with an ejection velocity of ~1 m s^{-1} will be about 2–20 g. Hayabusa2 sampling numerical simulations assuming a cohesionless granular bed consisting of grains with an average diameter of 0.5 cm predict that the total ejecta amount is about one order of magnitude larger than the amount of ejecta with an ejection velocity of ~1 m s^{-1} (*24*). The total ejecta mass is thus estimated to be 20–200 g. The simulation also predicts that about 0.5 % of the total ejecta particles are stored in the sample catcher located above the sampler horn (*24*). This leads to an estimated total collected mass of 0.1-1 g for TD1, more than the requirement for returned sample analysis (0.1 g) (*1, 21*). Laboratory experiments made at 1G with 1 mm-sized glass spherules with little cohesion force showed that 150–250 mg of samples can be collected as a result of the projectile shooting (fig. S2) (*23*), which is expected to be increased by at most one order of magnitude under microgravity conditions (*21*). Because the surface materials on Ryugu are not strongly stuck to the surface by cohesive forces (*19*), the on-ground experiment can be a good analogue of the sample collection operation on Ryugu. We conclude that the total collected mass of the samples through the projectile shooting from the two landing operations largely exceeded the requirement (0.1 g).

In the CAM-H images during TD2 (Fig. 2, movies S2 and S3), the clear detection of impact ejecta was not performed, but smoke-like ejecta was observed to emit from the sampler horn (Fig. 2) followed by the ejection of numerous larger particles. Three particles in Fig. 2 were found to be about 1-2 cm in diameter, suggesting that loosely packed movable centimeter-sized pebbles were present at the TD2 location. The CAM-H images suggests that a similar amount of material was expected to be collected in the TD2 operation as well.

A striking feature found in the TD2 location is the presence of fine particles on the surface of a boulder (Fig. 3), which was not confirmed in proximity images of TD1 and other surface locations (*9*). These particles were not adhered to the boulder because they were blown off by the thruster operation for the ascent (Fig. 3). The rarity of fine particles on the surface of smooth flat boulders is thus likely due to their short geological lifetime. Their presence on a boulder surface identified during TD2 must therefore be recent, suggesting that they are most likely ejecta from the SCI crater. As observed by the DCAM3 camera, part of the ejecta curtain produced by the SCI falls back on Ryugu's surface, leading to the TD2 site being covered with SCI ejecta. Experiments performed at 1G showed that ~50 % of the collected particles were from within the 1.5 mm depth from the surface (fig. S2) (*23*). Even with the enhanced collection efficiency under microgravity, which should allow accessing greater depth, the collected samples during TD2 should still include surface particles and therefore SCI ejecta.

The CAM-H continued to take images of flying particles during the ascent after the two landing operations (Fig. 4). Because no such particles were observed during the spacecraft descent, these particles are necessarily ejecta either due to the projectile impact or the thruster operation for the ascent. Observation of boulders moving on the surface due to the thruster operation by ONC-W1 (*9*) suggests that the thruster operation triggered ejection of most pebbles. Numerous millimeter-sized particles were also observed in the TD2 ascent operation (Fig. 4). This is also the evidence of the presence of small particles, including the SCI ejecta, at the TD2 location.

The flying pebbles show two morphological types: rugged particles and particles with smooth-faces (Fig. 4 and fig. S3). These two types are consistent with the morphological variations observed within surface boulders (*8*). The three-dimensional shape of flying pebbles was also determined for those showing multiple two-dimensional projections from different angles in CAM-H images. Maximum and minimum caliper lengths of the maximum-area projection of a particle were defined as L and I, and the smallest dimension measured in the minimum-area projection was defined as S (fig. S4) (*23, 25*). The S/L and I/L ratios of the particles (Fig. 4 and Tables S1 and S2) show that there is a fraction of elongated-block like flat particles on the surface. The probability distribution function of 67 particles shows a bimodal distribution centered at (S/L, I/L) of (0.53, 0.69) and (0.35, 0.48) (Fig. 5), meaning that two shape types are present in the population of surface pebbles (sub-equant and elongated blocks). Some pebbles and small boulders at the two landing locations are elongated and relatively flat in shape (Fig. 1). This suggests that the bimodal distribution of pebble shape is indigenous to Ryugu's surface. However, because such a bimodal distribution is not found for boulders larger than 5 meters (*26*), we conclude that boulder fragmentation is the origin of this shape variation. The elongated and flat pebbles may originate from layered boulders (Fig. 2) (*5*). The elongated and flat morphology is not typical of carbonaceous chondrites, but could be related to shocked hydrated carbonaceous chondrites (*27–30*). There are chondrites showing a high density of parallel fractures that formed due to sudden volatile loss during release of shock pressure (*30*).

CAM-H observed a centimeter-sized pebble that passed between the camera and the coupling ring in the TD1 ascent operation (Fig. 4). The pebble hit the spacecraft, and a smaller particle (~4 mm in size) appeared from the spacecraft side four seconds later. Because no other particle coming from the spacecraft side was observed during the TD1 and TD2 operations, the ~4 mm-sized particle should be a fragment of this centimeter-sized pebble, resulting from its impact with the spacecraft. The relative velocity of the pebble to the spacecraft was ~0.1 m/s. Its fragmentation at impact implies either that a tensile strength of the pebble is much smaller than that of typical chondrites (fig. S6) (*17, 23*) or that the pebble contained a crack (or cracks) as the boulder with a crack observed by the MINERVA-II-1B rover (Fig. 3).

Hayabusa2 left the asteroid in November 2019, and delivered its reentry capsule on December 6, 2020 to Woomera, South Australia. No damage to the reentry capsule was observed on ground, and the capsule was transported to the Quick Look Facility (QLF) in the Woomera Prohibited Area. The temperature monitor attached to the sample container, inside the reentry capsule, showed that the container was never heated up to 65°C, lower than the daytime temperature of the Ryugu surface. After the extraction of volatiles inside the sample container at the QLF (*22*), the sample container was transported to the curation facility at ISAS/JAXA using a nitrogen-purged anti-vibration transportation box (~57 hours after the capsule landing). The sample container, of which lid was pressed with a load of ~2700 N through pressure springs (*21*),

was installed into the container opening system to be opened in the clean chamber designed for Ryugu samples (*31*). The sample container with the opening system was attached to the clean chamber on December 11, 2020 and was opened in vacuum after the chamber evacuation for ~2.5 days (fig. S7).

Inside two separate chambers (chambers A (24 cm^3) and C (12 cm^3)) of the sample container (fig. S7), used for TD1 and TD2, millimeter-sized sands and nearly centimeter-sized pebbles were found with submillimeter-sized fine powder. The grain size variation is consistent with the surface observation by the MASCOT lander (*16, 17*), MINERVA-II rovers, cameras (ONC-W1, ONC-W2, and CAM-H) (Figs. 2–4), and polarimetric observations from ground (*32*). All the particles in the two chambers were black in color (Fig. 6), consistent with the color of Ryugu boulders (*8, 9*). Because only a small amount of fine particles (smaller than 1 mm) were found in the chamber B, which was not used for the landing operations, between the chambers A and C, the pebbles and sands in the chambers A and C are the samples acquired in the TD1 and TD2 operations, respectively. This also shows that no extensive mixing of particles occurred through the gaps between the chambers (*21*) and that the samples from two surface sites were kept separately throughout the Earth return operation.

The total weights of the particles were 3.2, <0.1, and 2.0 g for the chamber A (TD1), B, and C (TD2), respectively, consistent with the estimate from the CAM-H images (Fig. 4). The particles in the chambers are thus ejecta obtained by the projectile shooting onto the surface. The total amount of the sample exceeds the mission requirement for scientific analysis (0.1 g) (*1, 21*). The size of collected particles is also consistent with that of ejecta observed at each landing operation (Fig. 2). The largest grains in the chamber A are ~5 mm in size, while there are three pebbles larger than 5 mm in the chamber C (Fig. 6 and Table S3). The longest dimension of the largest pebble in the chamber C is 10.3 mm, which is close to the maximum obtainable size by the Hayabusa2 sampler (*21*). The presence of large pebbles in the chamber C, in spite of the smaller total weight, can be explained either by impact destruction of a boulder or by effective sampling of pebbles using a scoop-up part of the sampler horn at the TD2 site, which was designed to pick up surface pebbles (*21*). There are also millimeter-sized fine pebbles and sub-millimeter-sized sand particles in the chamber C, among which sub-surface material (Fig. 3) is likely to be included.

More than two hundred pebbles (1–10 mm in size) from the chambers A (79) and C (84) were individually picked up and observed under optical microscope (Fig. 6). The pebbles show morphological variation, and there are grains with ragged surface and with smooth surfaces (Fig. 6), consistent with that of flying pebbles observed during the TD1 and TD2 operations. Although detailed three-dimensional morphological investigation is not currently possible for individual grains in the clean chamber, there are elongated block-like pebbles in the collected sample (Fig. 6) and the S/L and I/L ratios of the pebbles are consistent with the flying particles observed at Ryugu (Fig. 5).

Many particles are found to contain curved and straight cracks. Pebbles with smooth surface may be fragments of particles with straight cracks. This observation suggests that the particle that was broken due to collision with the spacecraft (Fig. 4) contained a crack(s). The common presence of cracks in returned pebbles implies that the small thermal inertia of surface boulders (*17, 18*) is due to cracks/fractures in their interior.

All the physical properties, such as color, shape, and structure, of returned pebbles and sands match those of Ryugu surface material. We thus conclude that the pebbles and sands inside the chambers A and C are representative samples of the Ryugu surface material at two surface sites. The variations of physical properties among the pebbles and sands reflect the geological history of Ryugu (*1*) that will be investigated in the highest achievable level of accuracy by their analysis after the 6 month curatorial work without exposure to the air.

References and Notes:

1. S. Tachibana et al., Hayabusa2: Scientific importance of samples returned from C-type near-Earth asteroid (162173) 1999 JU_3. *Geochem. J.* **48**, 571–587 (2014).
2. A. Tsuchiyama et al., Three-dimensional structure of Hayabusa samples: Origin and evolution of Itokawa regolith. *Science* **333,** 1125–1128 (2011).
3. T. Noguchi et al., Incipient space weathering observed on the surface of Itokawa dust particles. *Science* **333,** 1121–1125 (2011).
4. K. Nagao et al., Irradiation history of Itokawa regolith material deduced from noble gases in the Hayabusa samples. *Science* **333,** 1128–1131 (2011).
5. E. Nakamura et al., Space environment of an asteroid preserved on micrograins returned by the Hayabusa spacecraft. *Proc. Natl. Acad. Sci. USA* **109,** E624–E629 (2012).
6. T. Matsumoto et al., Nanomorphology of Itokawa regolith particles: Application to space-weathering processes affecting the Itokawa asteroid. *Geochim. Cosmochim. Acta* **187,** 195–217 (2016).
7. S. Watanabe et al., Hayabusa2 arrives at the carbonaceous asteroid 162173 Ryugu—A spinning top-shaped rubble pile. *Science* **364**, 268–272 (2019).
8. S. Sugita et al., The geomorphology, color, and thermal properties of Ryugu: Implications for parent-body processes. *Science* **364**, eaaw0422 1-11 (2019).
9. T. Morota et al., Sample collection from asteroid (162173) Ryugu by Hayabusa2: Implications for surface evolution. *Science* **368,** 654–659 (2020).
10. E. Tatsumi et al., Collisional history of Ryugu's parent body from bright surface boulders. *Nature Astronomy* **5,** 39–45 (2020).
11. K. Kitazato et al., The surface composition of asteroid 162173 Ryugu from Hayabusa2 near-infrared spectroscopy. *Science* **364**, 272-275 (2019).
12. D. S. Lauretta et al., The unexpected surface of asteroid (101955) Bennu. *Nature* **568,** 55–60 (2019).
13. V. E. Hamilton et al., Evidence for widespread hydrated minerals on asteroid (101955) Bennu (2019). *Nature Astronomy* **3,** 332-340.
14. A. A. Simon et al., Widespread carbon-bearing materials on near-Earth asteroid (101955) Bennu. *Science* 10.1126/science.abc3522 (2020).
15. H. H. Kaplan et al., Bright carbonate veins on asteroid (101955) Bennu: Implications for aqueous alteration history. *Science* 10.1126/science.abc3557 (2020).
16. R. Jaumann et al., Images from the surface of asteroid Ryugu show rocks similar to carbonaceous chondrite meteorites. *Science* **365**, 817–820 (2019).
17. M. Grott et al., Low thermal conductivity boulder with high porosity identified on C-type asteroid (162173) Ryugu. *Nature Astronomy* **3,** 971–976 (2019).
18. T. Okada et al., Highly porous nature of a primitive asteroid revealed by thermal imaging. *Nature* **579,** 518–525 (2020).

19. M. Arakawa et al., An artificial impact on the asteroid 162173 Ryugu formed a crater in the gravity-dominated regime. *Science* **368**, 67–71 (2020).
20. K. Kitazato et al., Thermally altered subsurface material of asteroid (162173) Ryugu. *Nature Astronomy* (2021). doi.org/10.1038/s41550-020-01271-2
21. H. Sawada et al., Hayabusa2 sampler: Collection of asteroidal surface material. *Space Sc. Rev.* **208**, 81–106 (2017).
22. R. Okazaki et al., Hayabusa2 sample catcher and container: Metal-seal system for vacuum encapsulation of returned samples with volatiles and organic compounds recovered from C-type asteroid Ryugu. *Space Sci. Rev.* **208,** 107–124 (2017).
23. Materials and methods are available as supplementary materials.
24. F. Thuillet et al., Numerical modeling of medium-speed impacts on a granular surface in a low-gravity environment Application to Hayabusa2 sampling mechanism. *Month. Not. R. Astron. Soc.* **491,** 153–177 (2019).
25. T. Michikami et al., Boulder size and shape distributions on asteroid Ryugu. *Icarus* **331,** 179-191.
26. G. H. Bagheri et al., On the characterization of size and shape of irregular particles. *Powder Technol.* **270,** 141–153 (2015).
27. M. E. Zolensky et al., CM chondrites exhibit the complete petrologic range from type 2 to 1. *Geochim. Cosmochim. Acta* **61,** 5099–5115 (1997).
28. A. E. Rubin, Collisional facilitation of aqueous alteration of CM and CV carbonaceous chondrites. *Geochim. Cosmochim. Acta* **90,** 181–194 (2012).
29. R. D. Hanna et al., Impact-induced brittle deformation, porosity loss, and aqueous alteration in the Murchison CM chondrite. *Geochim. Cosmochim. Acta* **171,** 256–282 (2015).
30. T. Nakamura et al., Irradiation-energy dependence of the spectral changes of hydrous C-type asteroids based on 4 keV and 20 keV He exposure experiments of Murchison CM chondrite. 51st Lunar Planet. Sci. Conf. Abstract# 1310 (2020).
31. T. Yada et al., Handling and description of C-type asteroid Ryugu samples returned by Hayabusa2. 52nd Lunar Planet. Sci. Conf. Abstract# 2008 (2021).
32. D. Kuroda et al., Implications of high polarization degree for the surface state of Ryugu. *Astrophys. J. Lett.* **911,** L24 (6 pp).

Acknowledgments:

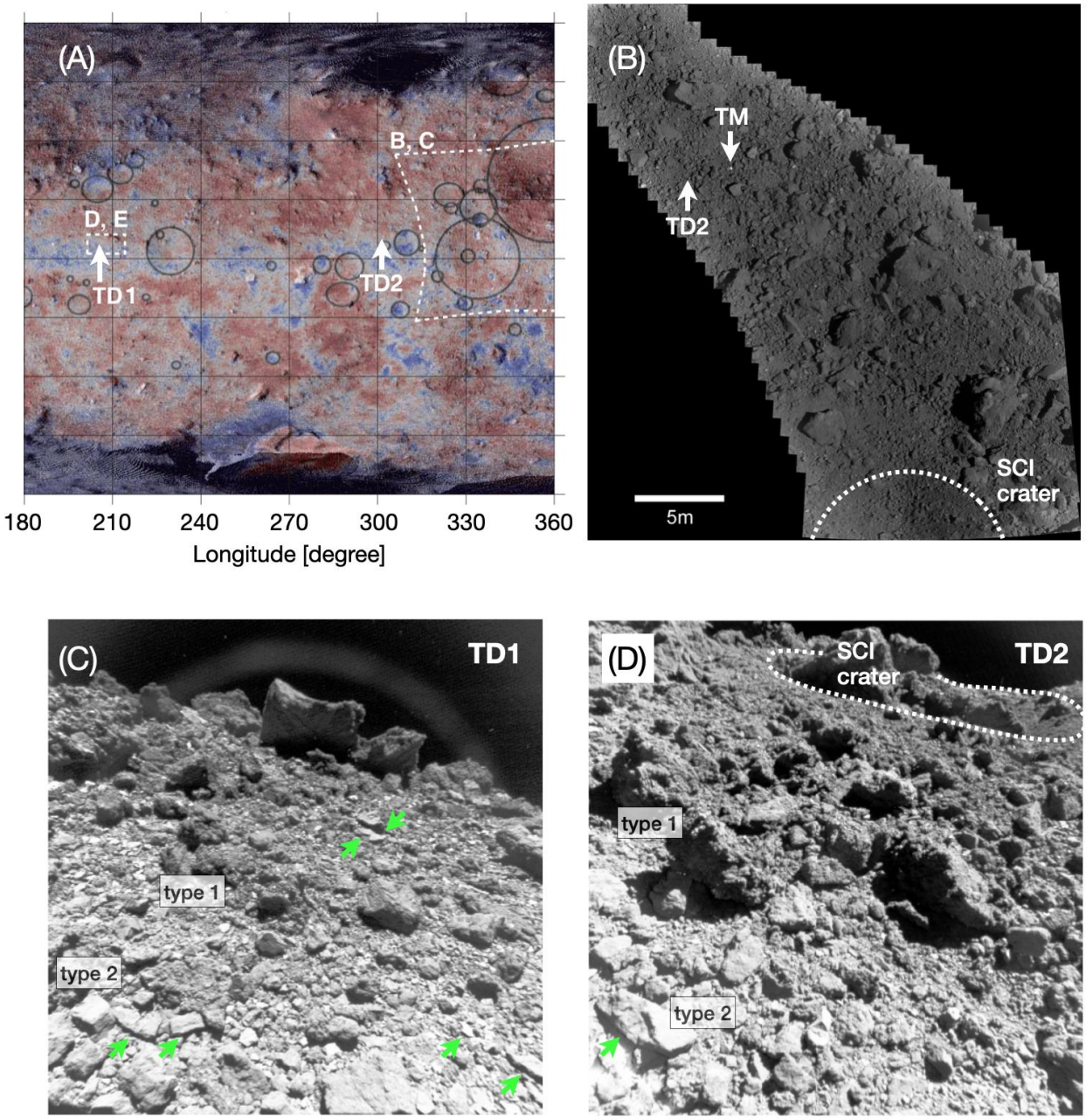

Fig. 1. **Hayabusa2 touchdown locations and surface conditions.** (**A**) A global map of the *b*-*x* slope (μm^{-1}), indicated by the color bar, superimposed on a *v*-band image map. The white arrows indicate the locations of the first touchdown (TD1) and the second touchdown (TD2). (**B**) TD2 site shown with the location of a target marker (TM) and the artificial crater produced by the SCI experiment[19]. The composite image was made from the images taken by ONC-W1. (**C**) (**D**) ONC-W2 images of the surrounding area of TD1 and TD2 sites, respectively. Flattened boulders/pebbles are indicated by yellow-green arrows.

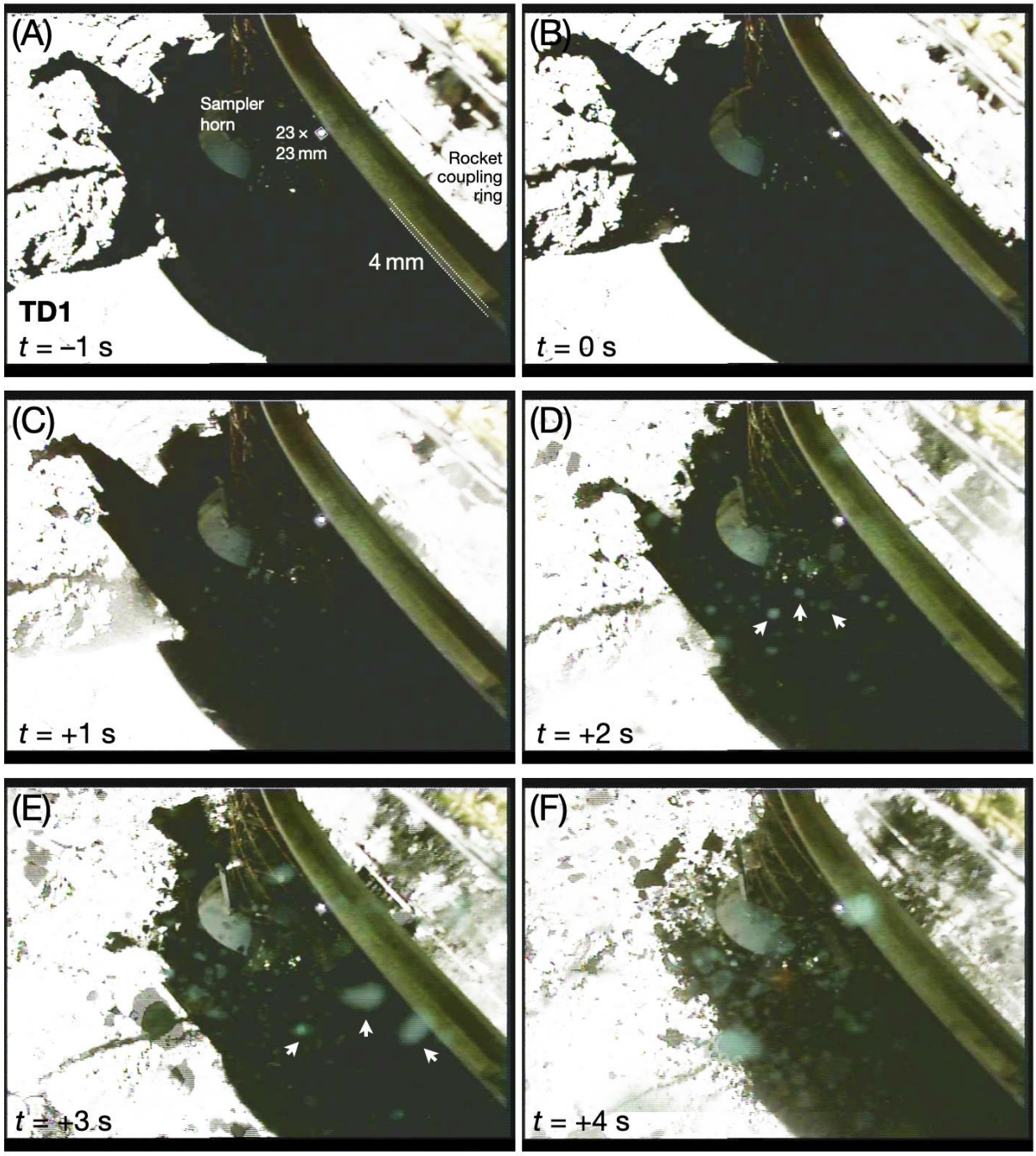
(A)
Sampler horn
23 × 23 mm
Rocket coupling ring
4 mm
TD1
t = –1 s
(B)
t = 0 s
(C)
t = +1 s
(D)
t = +2 s
(E)
t = +3 s
(F)
t = +4 s

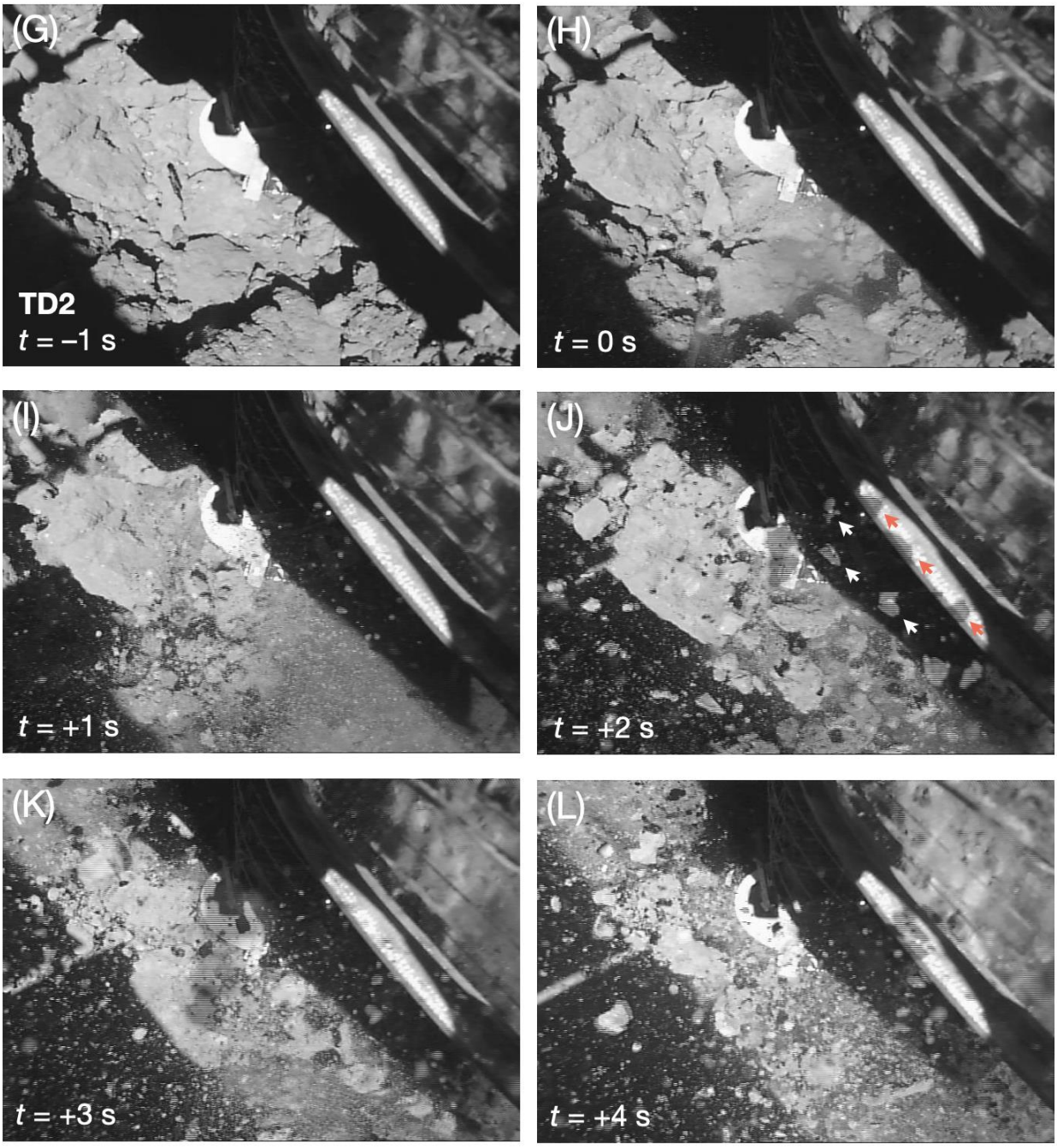

Fig. 2. **Images taken during TD1 and TD2 by a small monitor camera (CAM-H).** (**A**)–(**F**) The TD1 operation (–1 to 4 seconds from the touchdown). Ejecta particles are observed after the touchdown (t = 0 sec). The sizes of a reflection plate for a laser range finder (23 mm × 23 mm) on the sampler horn and a part of the rocket coupling ring (4 mm) are shown as a size reference. Particles indicated by white arrows in (**D**) and (**E**) are the same particles moving towards CAM-H. (**G**)–(**L**) The TD2 operation (–1 to 4 seconds from the touchdown). Mirror images of three particles, indicated by white arrows in (**J**), are seen on the rocket coupling ring (indicated by red arrows).

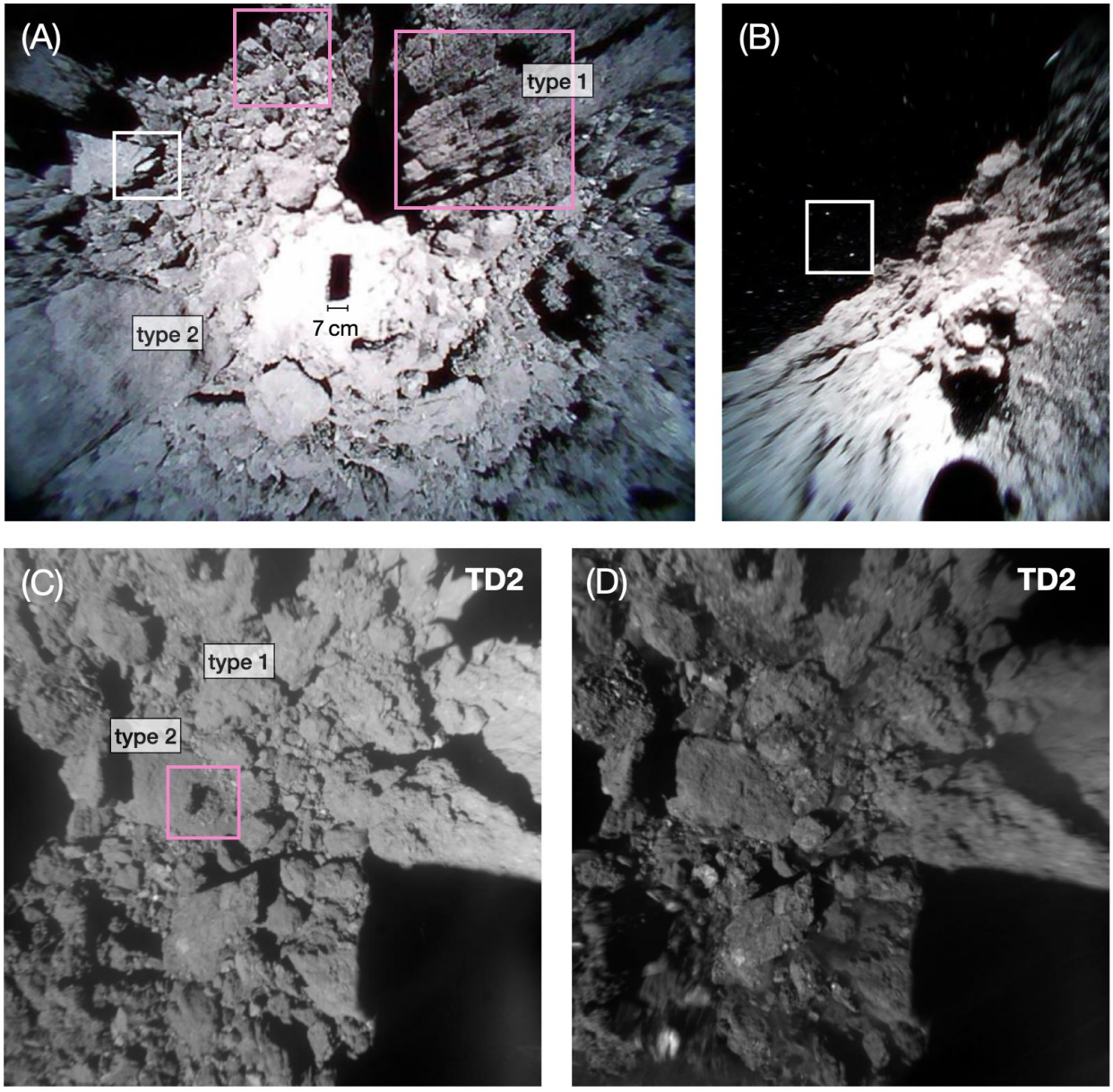

Fig. 3. Pebbles and structures of boulders observed on Ryugu's surface. (**A**) A surface image taken by the small rover MINERVA-II-1B during its hop (September 28, 2018). The shadow of the rover is shown in the center of the image. Numerous centimeter-sized pebbles are found in the image. Boulders with layered structure (pink boxes) and a boulder from which a flattened piece seems being peeled off (white box) are observed. Both type 1 and type 2 boulders[8], as in Fig. 1, are present in this region. (**B**) Ejected centimeter-sized pebbles associated with a hop of MINERVA-II-1B, taken on October 16, 2018. (**C**) Fine particles in a pink box on the surface of a smooth type 2 boulder just before TD2. Type 1 boulders are also observed in the area. (**D**) The same area shown in (**C**) after TD2. The fine particles on the smooth type 2 boulder were blown off due to the thruster operation for the spacecraft ascent.

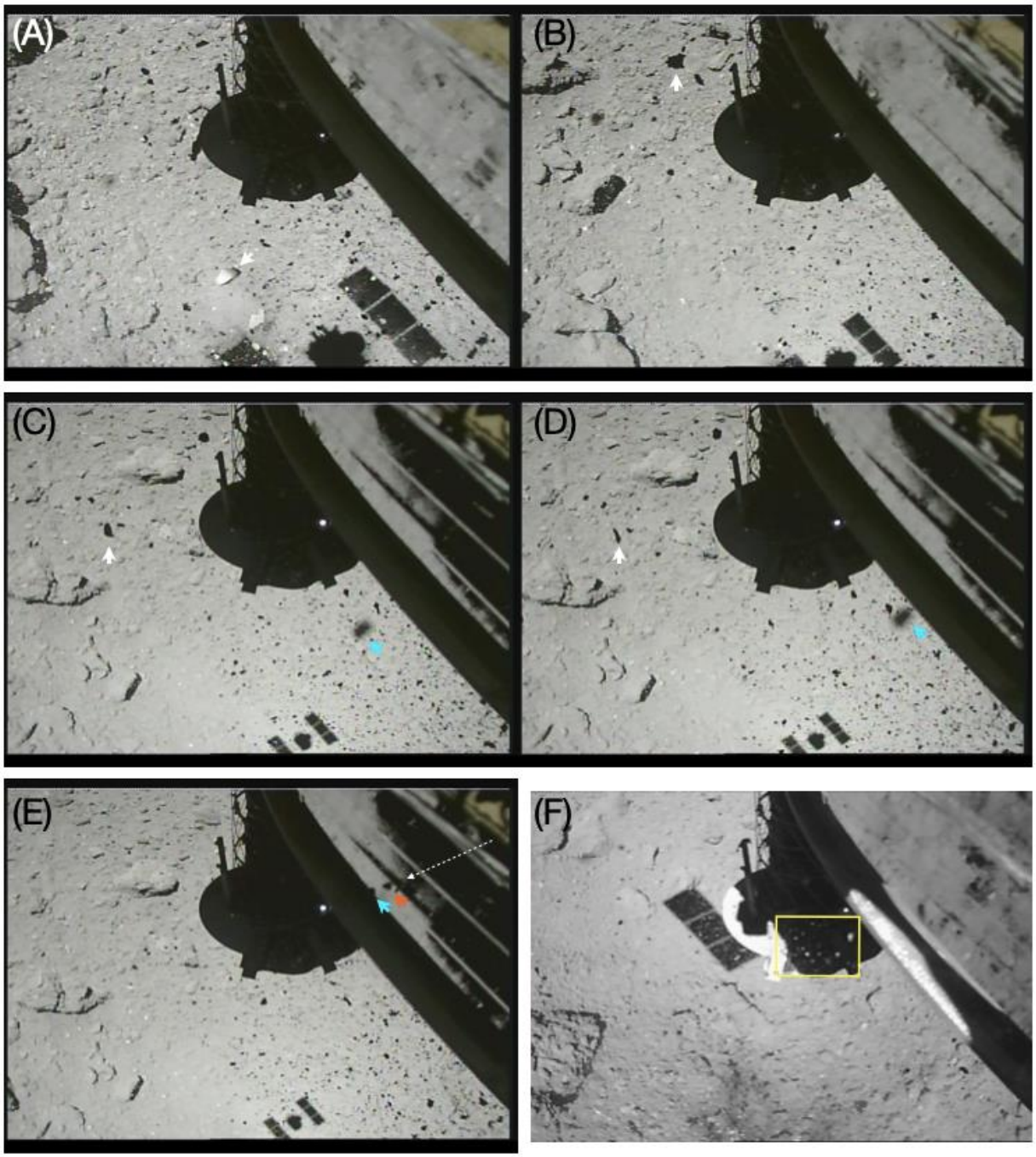

Fig. 4. Flying particles during the ascent after TD1 and TD2 and their morphological feature. (**A**) A particle with smooth faces (TD1), indicated by a white arrow. (**B**) A rugged particle (TD1), indicated by a white arrow. (**C**) (**D**) A flattened particle (white arrow) and a particle that was highly likely to have hit the spacecraft (blue arrow) (TD1). (**E**) A particle coming from the spacecraft side indicated by a blue arrow. Its mirror image is seen on the rocket coupling ring (red arrow). The moving direction of the particle is also shown with a white dotted arrow. (**F**) Millimeter-sized particles (shown in a yellow box) observed after TD2.

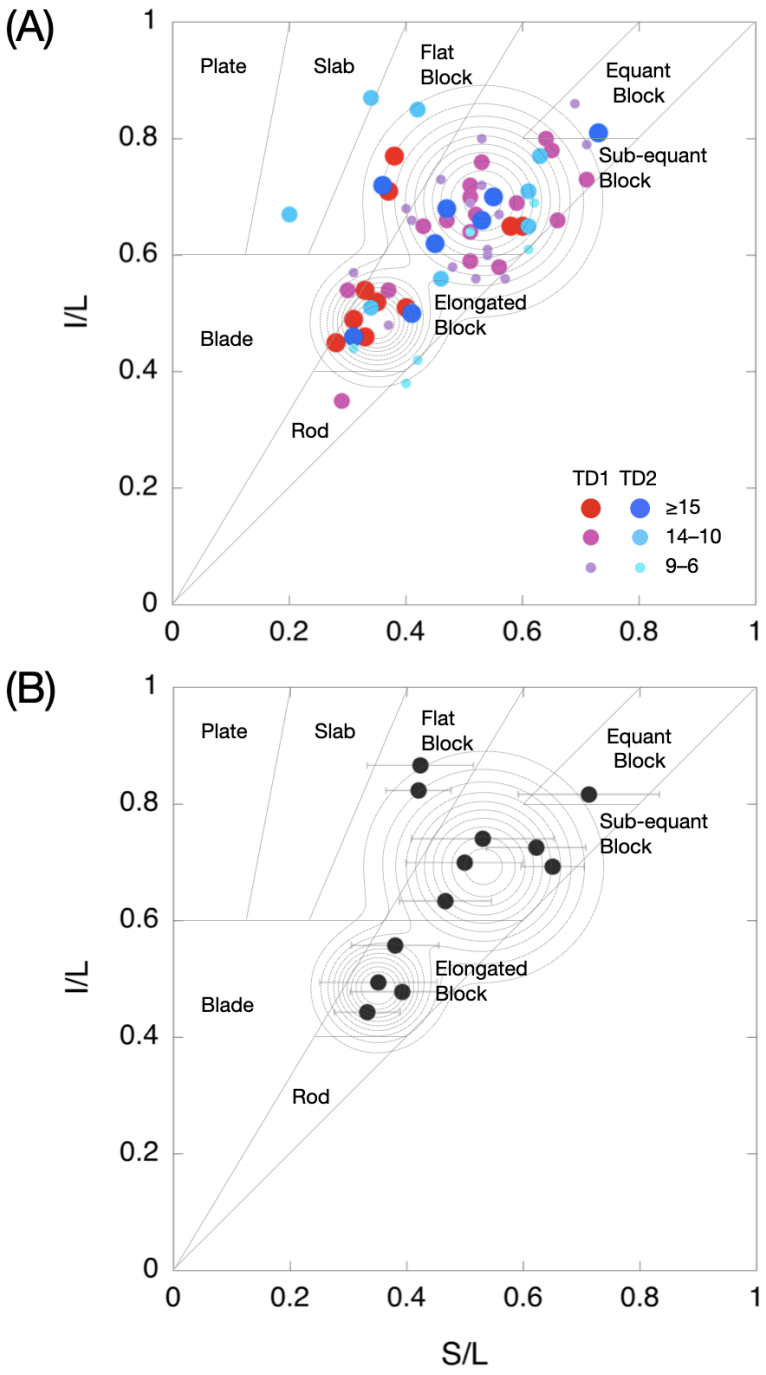

Fig. 5. Shape parameters of flying particles during touch-down operations and particles inside the sample catchers. (A) Particles observed by CAM-H during TD1 and TD2 operations. *S*/*L* and *I*/*L* denote the length ratios between the shortest and longest semimajor axes and between the intermediate and longest semimajor axes[23]. The probability distribution function of 67 particles is also shown as contours. **(B)** Estimated shape parameters of 6 and 6 particles from the chambers A and C of the sample catcher[23]. The particles in the sample catcher show a similar shape variation to the flying particles.

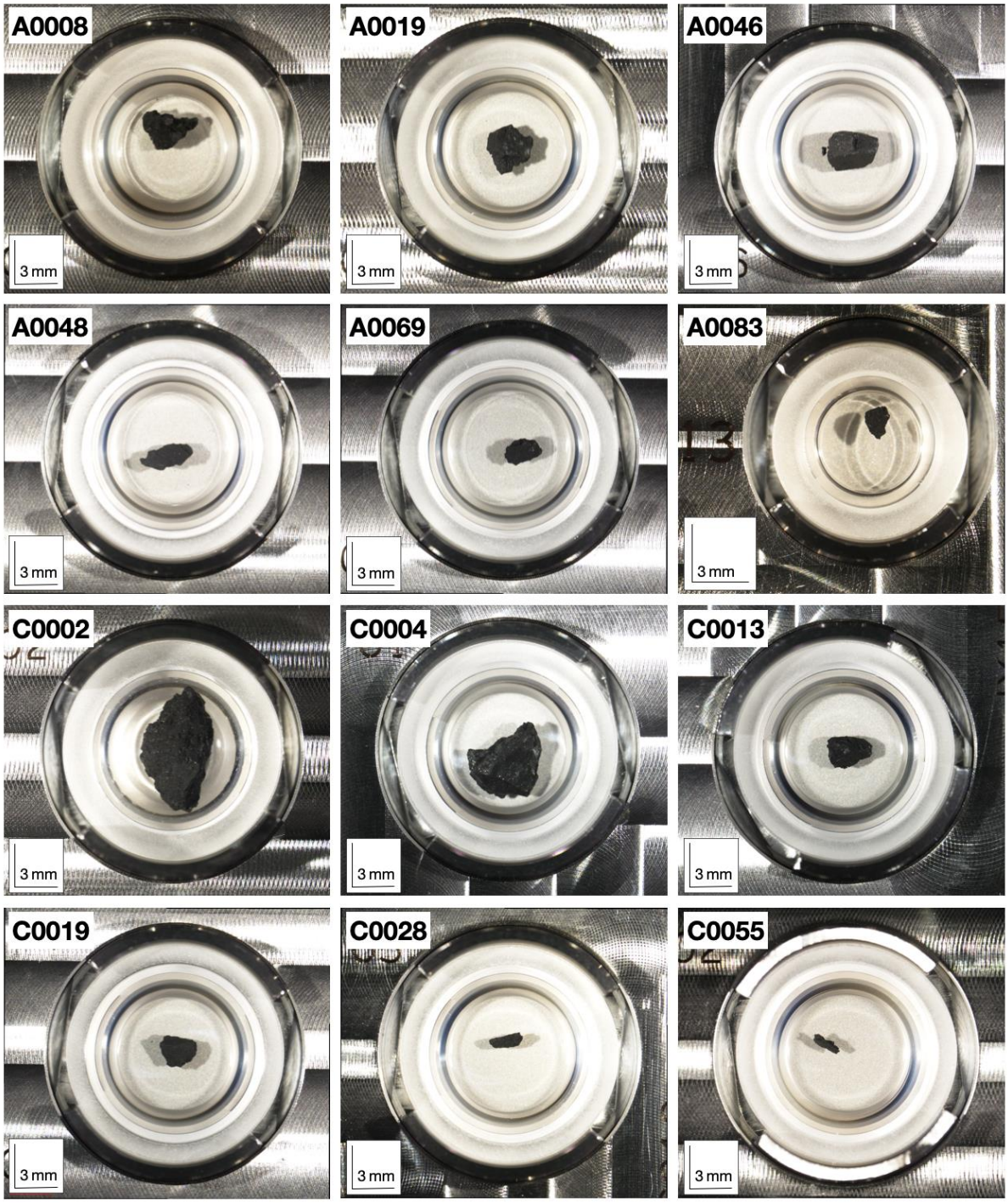

Fig. 6. Particles found inside the sample container. Particles A0008, A0019, A0046, A0048, A0069, and A0083 are from the chamber A of the sample container used for TD1, and C0002, C0004, C0013, C0019, C0028, and C0055 are from the chamber C of the sample container used for TD2. The particles A0008, A0019, A0069, A0083, and C0002 have rugged surfaces, while A0046 and C0019 have smooth surfaces. The particles A0048, C0028, and C0055 show elongated block-like morphologies.

Supplementary Materials:

Materials and Methods

Hayabusa2 sampler and sampling operation at Ryugu

The Hayabusa2 sampler consists of (1) a sample storage and transfer mechanism, (2) a 1-m long extendable sampler horn, and (3) a projector part (*1, 21, 22*), which was developed through modification from the Hayabusa sampler (*33*). A 5-gram tantalum projectile is shot through the sampler horn at an impact velocity of 300 m s^{-1} at the time of each touchdown, triggered by bending and/or shrinkage of the sampler horn (*21*). The firing of projectiles was confirmed for two landing operations through the temperature rise near the projector due to firing. Because Hayabusa did not fire projectiles on Itokawa (*21*), two landing operations of Hayabusa2 proved for the first time that the projectile-shooting sampling device works at the asteroid surface. The bottom end of the sampler horn is turned up to lift up surface pebbles (<~5 mm) during landing (*21*). The lifted pebbles were also expected to be stored in the sample catcher by deceleration of the spacecraft.

The ejecta from the surface is supposed to be put into a sample catcher through the sampler horn and a conical horn under microgravity conditions. The sample catcher has three chambers to store samples, acquired at different surface locations, separately (*21*). A rotatable inlet, connected to the conical horn, to the sample catcher was rotated after the first landing operation, and the samples obtained at TD1 and TD2 sites were stored in different chambers (chambers A and C (*21*)). The rotatable inlet was moved to the final position to close all the chambers after TD2.

On August 26, 2019, the sample catcher was transported into the sample container inside the Earth re-entry capsule and sealed successfully. The container sealing method adopted for Hayabusa2 is an aluminum metal seal, where the sample catcher is sealed in the sample container by deformation of the curved surface lid with the edge of the sample container (*22*). This sealing method allows only a leak of 1 Pa air for 100 hours at atmospheric pressure (*22*).

Sampling simulation experiments in one Earth gravity (1G)

On-ground laboratory experiments with the full-scale sampling device were performed in vacuum (40 ± 10 Pa) using 1-mm sized glass spherules to investigate the ejection behavior of particles, the collection efficiency of ejecta, and the collection efficiency of top-surface materials.

For ejection angle measurements, an aluminum plate with 5-mm wide slit was placed 10 mm above the surface to limit the direction of particle ejection. The ejection angle of most particles was within 40–60° (fig. S1), and particles from the area nearby the impact point tend to have higher ejection angles.

The experiments without the aluminum plate showed that the collection efficiency depends on the kinetic energy of the projectile. An amount of 150–250 mg of samples can be collected in the 1G environment for a projectile's kinetic energy at impact of ~225 J (fig. S2). It has been confirmed that the collection efficiency in microgravity is a few times to one order of magnitude larger than that at 1G because low-velocity ejecta can be effectively collected (*21*). Some experiments were done using colored glass beads for the top 1.5 mm layer to obtain the

collection efficiency of very surface material. The collection efficiency was found to be ~50 % for an impact kinetic energy of 225 J (fig. S3), suggesting that the SCI impact ejecta that fell back on Ryugu's surface should be collected at the TD2 site.

Hopping trajectory of MINERVA-II rovers and dust particle sizes on the surface of Ryugu

Two rovers, MINERVA-II-1A and -1B successfully landed on the surface of Ryugu on 21 September 2018 (*8*). The rovers hop on Ryugu's surface through rotation of their internal reaction wheel. The hopping trajectory of the rovers is here considered as a Keplerian motion around the center of Ryugu because of the small gravity of Ryugu (GM ~ 30 m^3 s^{-2}) (*7*). The Keplerian motion can be determined with the initial velocity of the rover (i.e., the sum of rover's hopping velocity and Ryugu's rotational velocity) and the distance between the center of Ryugu and the hopping location at the surface. We assume that the rover is located at the equator and that it hops toward east or west to simplify the effect of Ryugu's rotation on the rover trajectory.

Because of the law of constant areal velocity in the Keplerian motion, the speed (v_p) of the rover at its peak position during a hop and its height (l_p) from the Ryugu's center is connected with the initial velocity of the rover (v_h) relative to Ryugu's surface and its hopping elevation angle (θ_h) as;

$$\frac{1}{2} l_p v_p = \frac{1}{2} R v_0 \cos\theta_0, \text{(S1)}$$

where

$$v_0 = \sqrt{(v_R \pm v_h \cos\theta_0)^2 + (v_h \sin\theta_0)^2},$$

$$\theta_0 = \arctan\left(\frac{v_h \sin\theta_h}{v_R \pm v_h \cos\theta_h}\right),$$

and v_R is the rotation velocity of Ryugu, and R is the radius of Ryugu at the hopping location. Note that v_R is equal to $R \times 2\pi/(7.6 \times 60 \times 60)$ m s^{-1} (The denominator represents the Ryugu's rotation period in second). Here the sign of $v_h \cos\theta_h$ is positive for a prograde hop and negative for a retrograde hop. From the law of energy conservation,

$$\frac{1}{2} {v_0}^2 - \frac{GM}{R} = \frac{1}{2} {v_p}^2 - \frac{GM}{l_p}. \text{(S2)}$$

Equations (S1) and (S2) provide two sets of v_p and l_p, which correspond to those at a peak position of a hopping and those at another peak position in an ellipsoidal trajectory, respectively. Here we set v_{p1} and l_{p1} as the velocity and height at a peak position of a hop, and v_{p2} and l_{p2} for the other position. The semi-major radius (a) and the semi-minor radius (b) of the trajectory are given by:

$$a = \frac{1}{2}(l_{p1} + l_{p2}), \text{ (S3)}$$

$$b = \sqrt{a^2 - (a - l_{p2})^2}. \text{ (S4)}$$

The ellipse of the hopping trajectory in a polar coordinate system with the origin at the center of Ryugu can be expressed with

$$r(\lambda) = \frac{b^2}{a}\frac{1}{1+\varepsilon\cos\lambda}, \text{(S5)}$$

where

$$\varepsilon = \frac{-\sqrt{a^2-b^2}}{a}.$$

Since r=R when the rover hops,

$$\lambda_0 = \cos^{-1}\left\{\frac{1}{\varepsilon}\left(\frac{b^2}{aR}-1\right)\right\}. \text{(S6)}$$

where λ_0 is λ at the hopping position on the surface of Ryugu. The area that is swept by a line between a rover and the center of Ryugu during a hop can be written with

$$S_{hopping} = 2\int_0^{\lambda_0}\frac{1}{2}r(\lambda)r(\lambda+d\lambda)\sin d\lambda\,, \text{(S7)}$$

and the duration of a hop is given by

$$T_{hopping} = \frac{S_{hopping}}{\frac{1}{2}Rv_0\cos\theta_0}. \text{(S8)}$$

Through (S1) to (S8), we can determine the trajectory of the rover with the hopping duration, which is the only parameter we can obtain in the rover operation, with an assumption on the initial velocity. The direction of the hopping (i.e. the elevation angle of the hop) is determined from (S8).

The MINERVA-II-1A rover conducted hopping many times and took more than 100 images near and on Ryugu's surface. In addition, some images showed several regolith particles lifted from the asteroid surface, which is presumably induced by hops of the rover. Figure 3(B) shows an example of such images capturing regolith particles taken by Rover 1A with its wide-angle camera on October 16, 2018 (Sol 82). This image was taken 12 seconds after the rover hopped, and the duration of the hopping was recorded as 1024 ± 7 seconds.

At the equator, Ryugu's surface rotates at 11.2 cm s^{-1}, whereas the hopping velocity estimated based on the pre-launch experiments is < 10 cm s^{-1}. By substituting these speeds and the observed hopping duration into (S1)–(S8), we obtain the elevation angle θ_h of ~30°. Furthermore, based on the time between imaging and hopping, we can estimate that the horizontal distance between the origin of this hop and the rover position at the time of this imaging is ~1 m and that the altitude of the rover is ~0.5 m.

Since the rover hops by utilizing its rotational motion, the rotation velocity should be almost the same as the hopping velocity. The maximum ejection velocity of regolith particles lifted by the rover hopping is likely to be of the same order of magnitude as the hopping velocity.

The distance of lifted particles should thus be less than 2 m even in the farthest case. Because the apparent particle sizes are from 2–4 pixels (Fig. 2) and the angular resolution of the image is 0.175 degree/pixel based on the ground experiments, the particle sizes could be, or smaller than, 5–10 cm.

Particle shape analysis of flying particles

Three-dimensional shape parameters of irregular particles were determined from multiple projection images (fig. S4) taken by CAM-H following the protocol developed by (*26*). Maximum and minimum caliper lengths of the maximum-area projection of a particle were defined as L and I, which do not necessarily need to be measured perpendicularly to each other (*26*). The smallest dimension measured in the minimum-area projection was used as S. Because the distance between the spacecraft and the particle changes with time, the maximum and minimum area projections were chosen from images during the time interval when the particle projection area did not change monotonically with time or within a short time interval (a few seconds). The L, I, and S of flying pebbles, determined with ImageJ (NIH) (*34*), are listed in Tables S1 and S2 with the S/L and I/L ratios. The solidity (the area of a shape divided by the area of its convex hull) of individual particles, which was obtained as the average of the solidity for each projection is also listed with its 2-sigma standard deviation in Tables S1 and S2.

The reliability of this shape analysis was tested by determining S/L and I/L ratios from multiple projections of rotating ellipsoids with three semimajor axes of L', I', and S'. Four sets of (S'/L', I'/L') were considered in this study; (S'/L', I'/L') = (0.431, 0.641), (0.3, 0.5), (0.2, 0.7), and (0.6, 0.7). The (S'/L', I'/L') of (0.431, 0.641) corresponds to the average axis ratio of particles after isotropic fragmentation (*34*). The other three sets represent elongated, flat, and equant particles, respectively. In the simulation with Mathematica (Wolfram), the direction of the spin axis was randomly selected against the semimajor axes of an ellipsoid and the projection direction. Different numbers of projections (n = 20, 12, 6, and 3), which were made by randomly changing the rotation angle around the spin axis, were used to determine S/L and I/L. The calculation of S/L and I/L was repeated 10^5 times for individual sets of L', I', S' and n.

The frequency distributions of evaluated S/L and I/L ratios are shown in fig. S5. The simulation shows that the obtained I/L ratio well corresponds to I'/L' even if n is 3, and that the S/L ratio is well determined for $n > 10$ and reasonably well for $n = 6$ (fig. S5). We thus used the S/L and I/L ratios of individual particles with the number of projections larger than 6 (Tables S1 and S2) for further discussion on the particle shape (Fig. 4). We note that the discussion on particle shape in the main text is not affected even if we include the data for eight particles with the number of projections of 5.

Particle shape analysis of particles in the sample catcher

Particles in the chambers A and C of the sample catcher were transferred to three sapphire glass dishes (six dishes in total), respectively. Individual particles were picked up from the dishes using vacuum tweezers (*31*) for optical investigation in a nitrogen-purged clean chamber without exposure to the air. The optical observation was made with a stereo microscope (Nikon SMZ1270i) through the window of the clean chamber. The maximum and minimum caliper lengths of the particle were obtained from its projection image using ImageJ (NIH) (*34*).

The uncertainty of caliper length measurement (Table S3) is given as six-pixel lengths of each image considering the dimness of the particle periphery. The particle height was given as the vertical distance from the dish floor to the top of the particle by changing the focal point of the microscope. The focal depth of the objective lens was used as the height uncertainty (Table S3). We note that the shape analysis here was done only from one direction due to limitation of particle handling in the clean chamber and further observation should be done for the precise shape analysis.

Particle destruction experiments

Destruction experiments of sintered glass beads and simplified Ryugu simulants (*36*), of which tensile strengths are similar to carbonaceous chondrites (1 to a few MPa) were performed by dropping round- and blocky-shaped samples from different heights (0.1–7 m) at one Earth gravity. The impact velocities ranged from 1.4–12 m s^{-1}. The sample size and mass ranged from ~1–6 cm and 0.5–25 g, respectively. Catastrophic destruction of most samples occurred when the impact velocity was >5 m s^{-1} (fig. S6). Only one sample out of 56 samples was fragmented at the impact velocity of 1.4 m s^{-1}. This implies that the tensile strength of the fragmented particle observed by CAM-H (Fig. 4) was much smaller than that of typical carbonaceous chondrites or there was a crack inside the particle.

Ground-based assessments of the projector system before/after touchdown operation

The ground-based rehearsal for Ta-projectile shooting operation was conducted under a low pressure condition using the identical flight model (*21*) with the Ryugu simulants (*36*) on December 28, 2018 prior to the TD1 operation. For the purpose of quality verification over the 4-year storage time, we also assessed a nominal operation of the projector system, including a double-check of interior explosives within the entire configuration (*21*). The projectile shooting was successfully performed without any defect of the configuration in the projector device (Movie S4). Because the nominal operation was completed along with the procedure (*21*), we expect that the issues of quality assurance for indigenous Ryugu sample has been secured (*37*).

The second ground-based projectile shooting operation was made with the Ryugu simulants (*36*) on March 15, 2021. The projectile was shot on a 15 cm-sized block. The projectile penetrated and fractured the block, associated with ejection of centimeter- to millimeter-sized fragments and fine dust (fig. S7). Platy particles were also observed in the ejecta (fig. S7). Centimeter-sized pebbles in the chamber C could be fragments of a larger boulder on the Ryugu surface. The future analysis of pebbles may reveal the original boulder surface and newly exposed fractured faces.

References

33. H. Yano et al., Touchdown of the Hayabusa Spacecraft at the Muses Sea on Itokawa. *Science* **312**, 1350–1353 (2006).
34. C. A. Schneider et al., NIH Image to ImageJ: 25 years of image analysis. *Nature methods* **9,** 671-675 (2012).
35. G. Domokos et al., Universality of fragment shapes. *Sci. Rep.* **5,** 9147 (6 pp) (2015).

36. H. Miyamoto and T. Niihara, Simplified simulated materials of asteroid Ryugu for spacecraft operations and scientific evaluations. *Nat. Resour. Res.* (10 pp) (2020). doi.org/10.1007/s11053-020-09626-2
37. Y. Takano et al., Chemical assessment of the explosive chamber in the projector system of Hayabusa2 for asteroid sampling. *Earth Planets Space* **72,** Article number: 97 (2020). doi:10.1186/s40623-020-01217-y

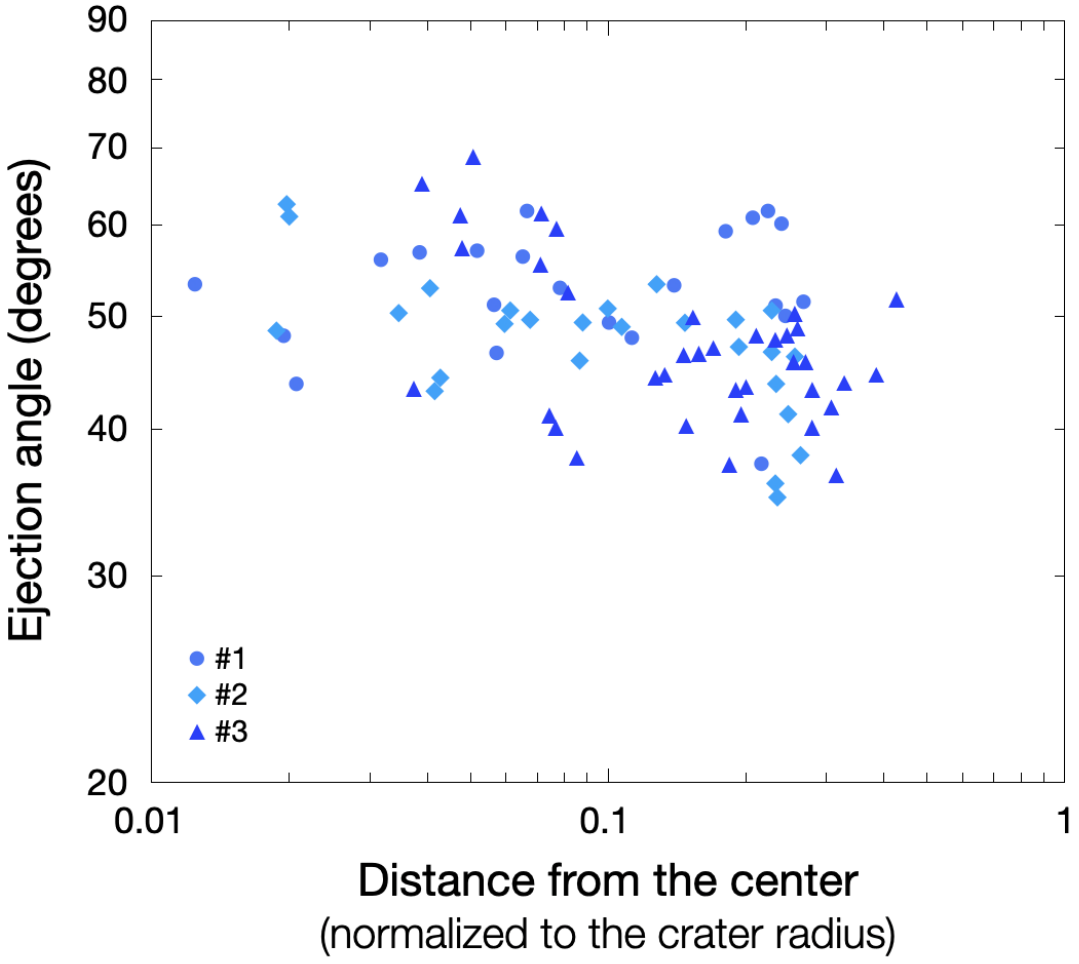

fig. S1. Ejection angle of individual particles as a function of the distance (*X*) from the impact point for three impact experiments in Earth's gravity (1G). The distance (*X*) is normalized to the radius of the impact crater (*R*).

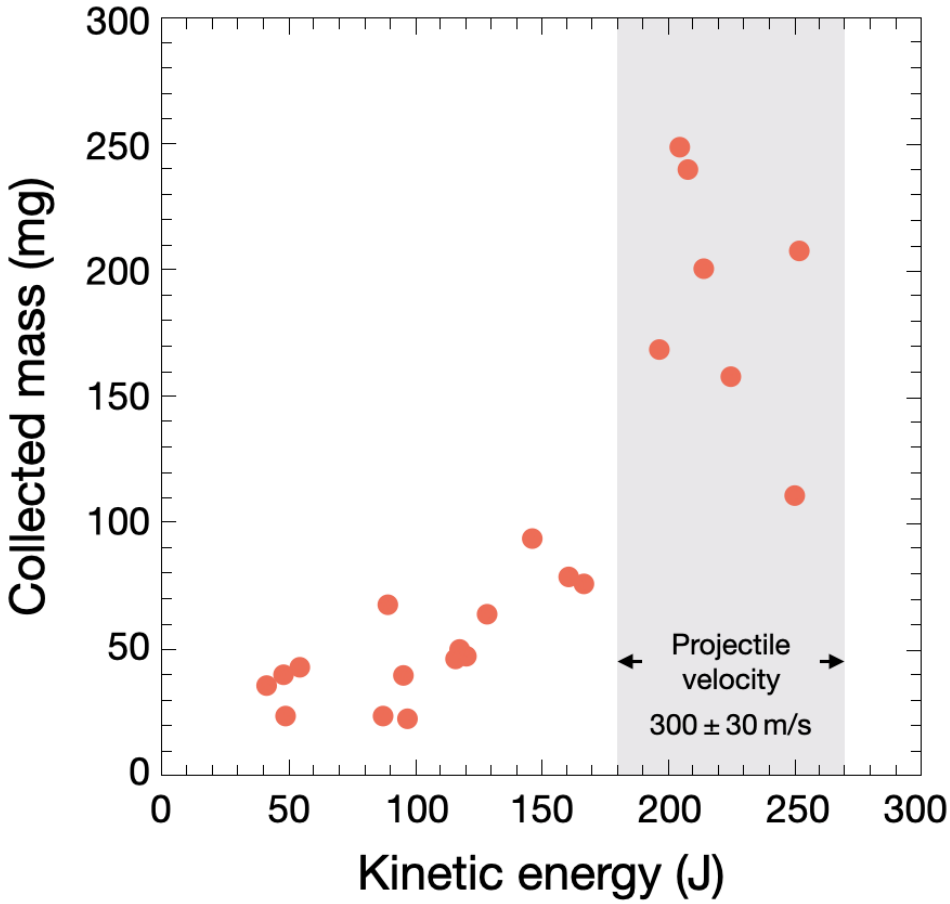

fig. S2. The total mass of collected glass spherules in 1G impact experiments with different kinetic energies of the projectile. The kinetic energy of the projectile from the Hayabusa2 sampler is ~225 J.

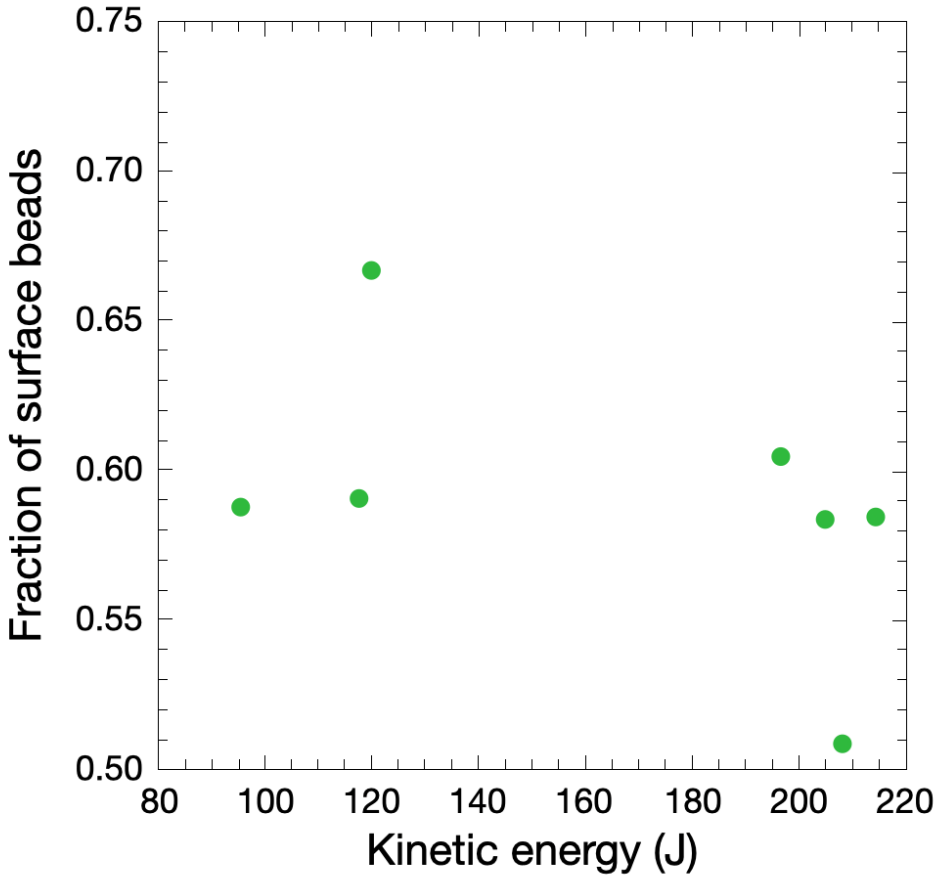

fig. S3. The fraction of particles collected within the 1.5 mm depth from the surface for different impact kinetic energies. The kinetic energy of the projectile from the Hayabusa2 sampler is ~225 J.

1-29

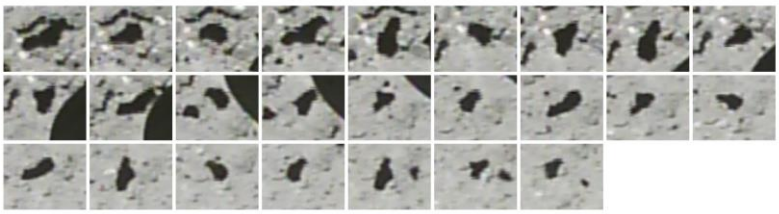

1-49

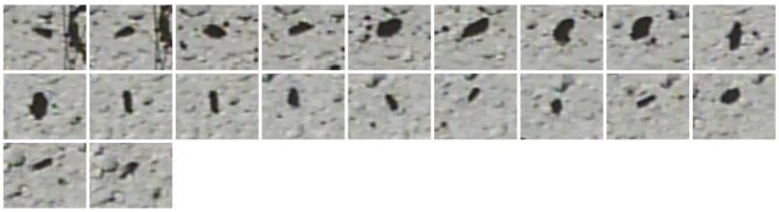

1-66

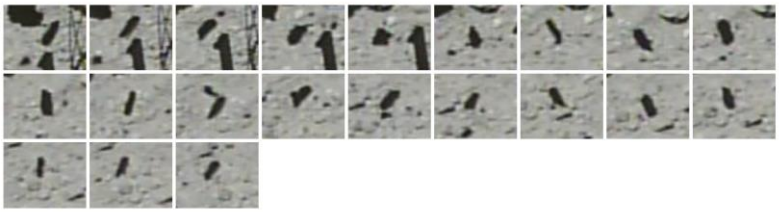

1-74

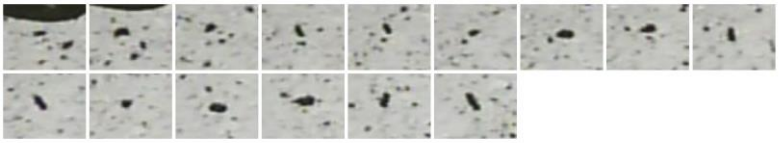

1-76

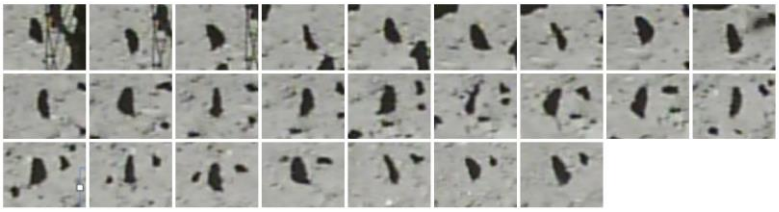

1-79

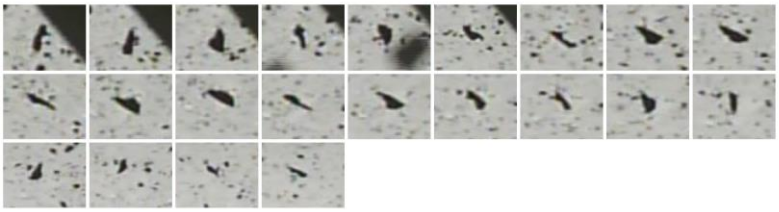

1-78

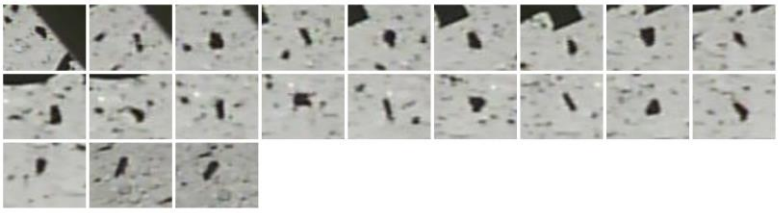

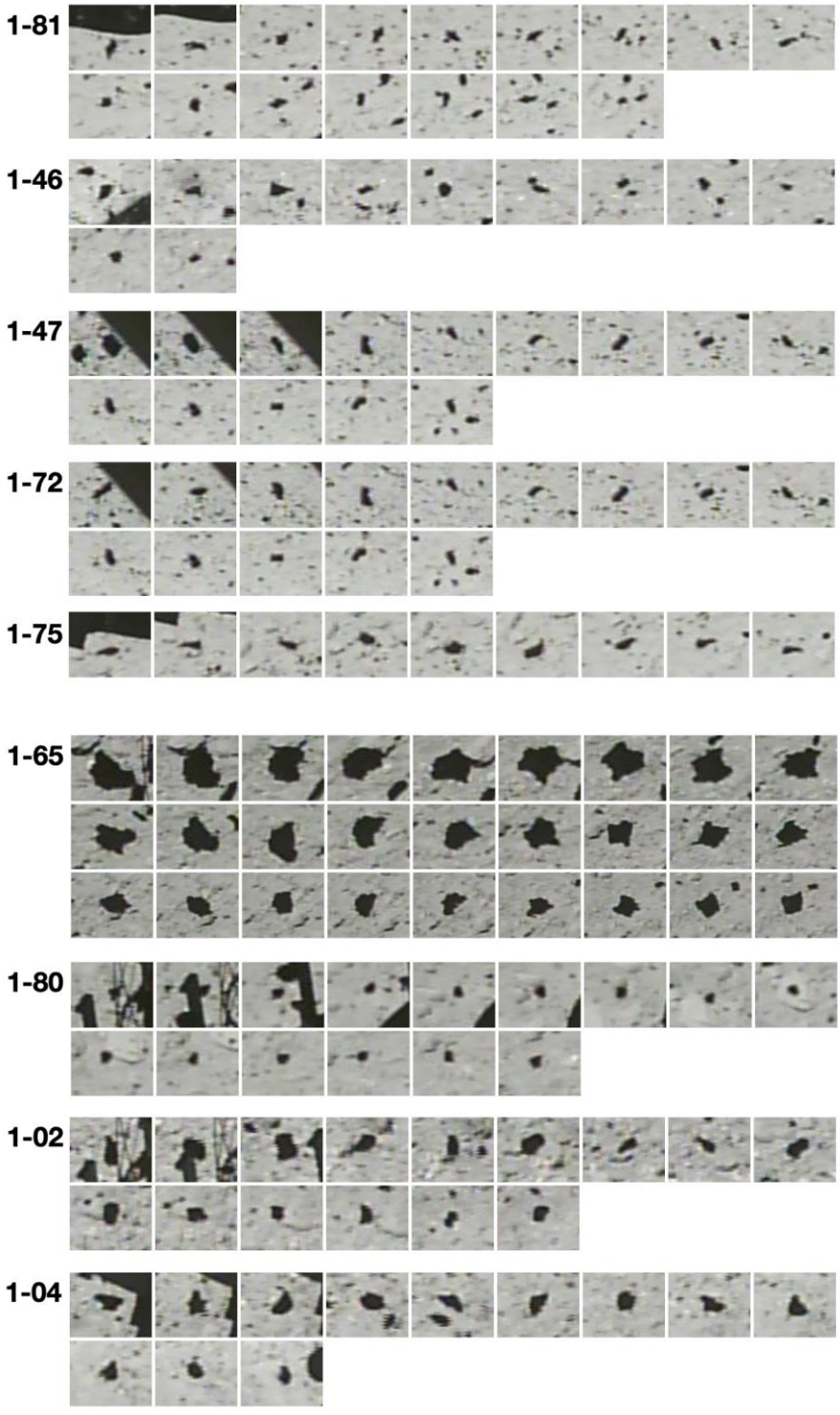
1-81
1-46
1-47
1-72
1-75
1-65
1-80
1-02
1-04

1-05

1-07

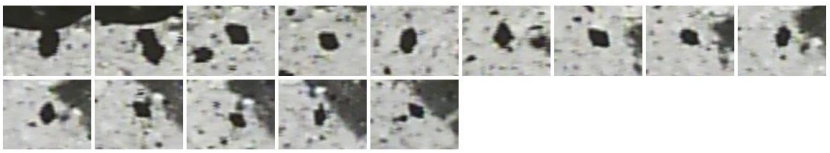

1-22

1-39

1-40

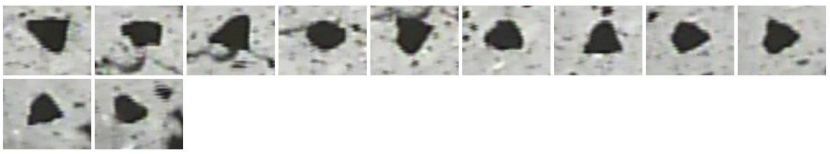

1-44

1-55

1-06

1-64

1-71

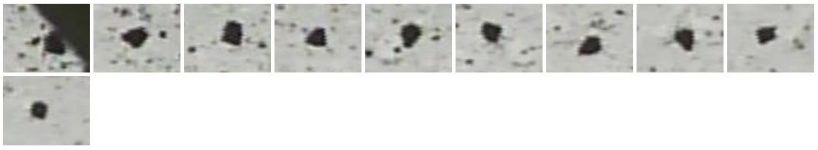

1-77

1-82

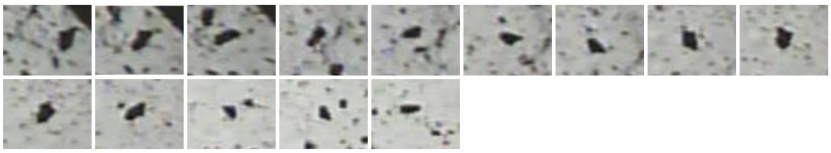

2-19

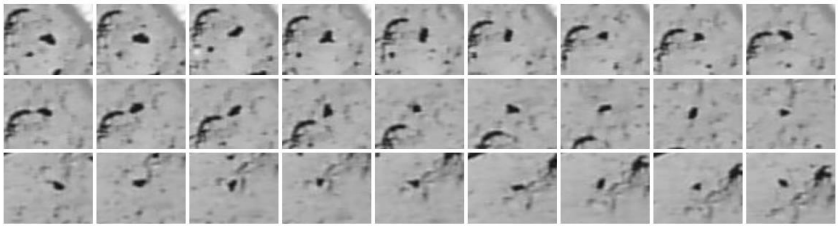

2-29

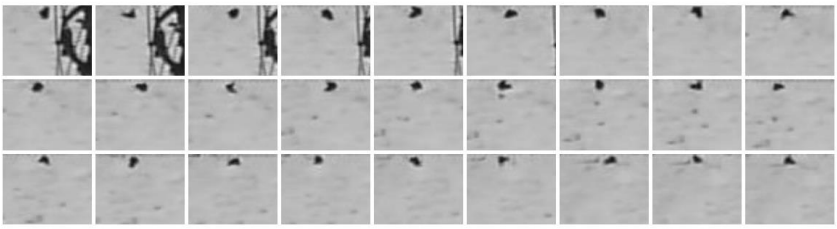

2-20

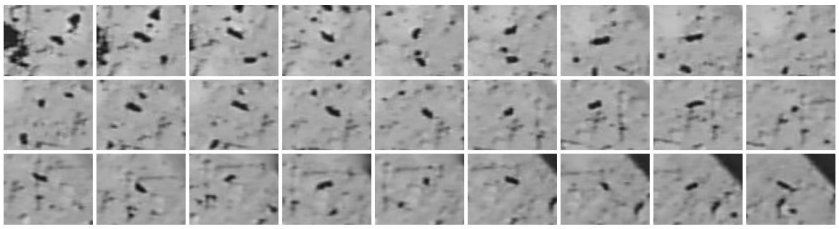

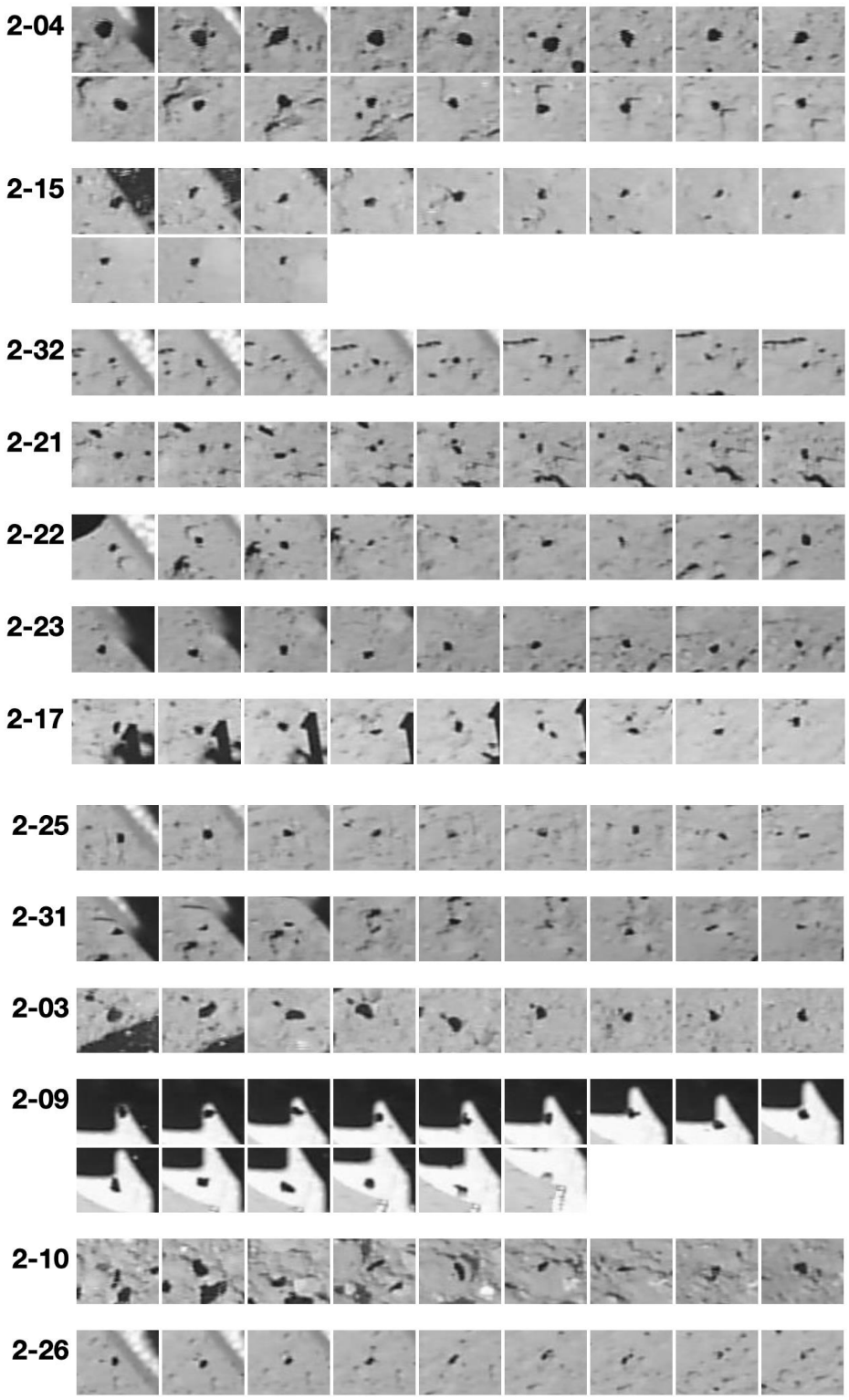

fig. S4. Time sequence images of flying particles taken by CAM-H during TD1 and TD2 operations. The form parameters (*S*/*L* and *I*/*L*) were determined for these particles with multiple images (Tables S1 and S2).

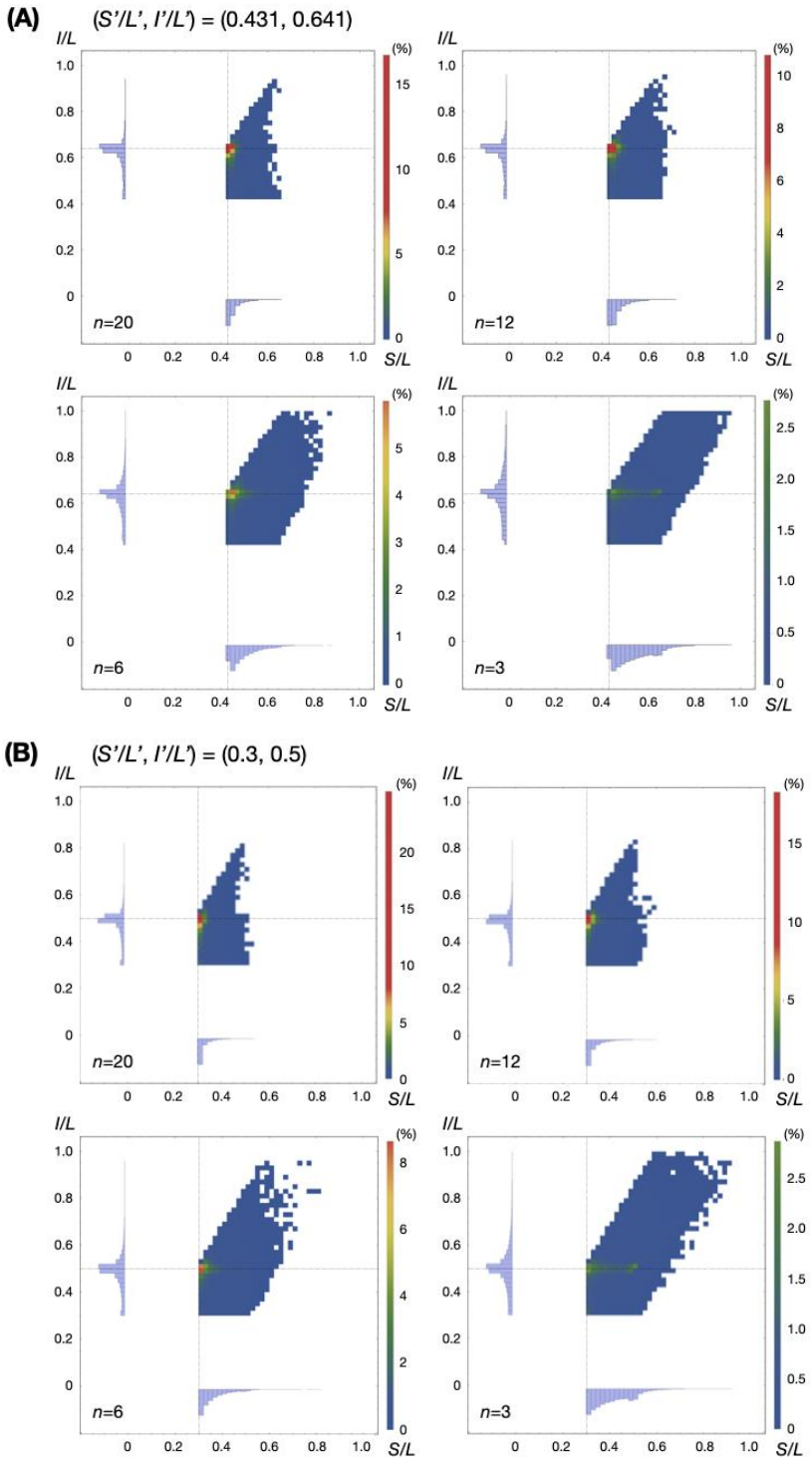
(A)
(S'/L', I'/L') = (0.431, 0.641)
I/L
S/L
(%)
n=20
n=12
n=6
n=3
(B)
(S'/L', I'/L') = (0.3, 0.5)
I/L
S/L
(%)
n=20
n=12
n=6
n=3

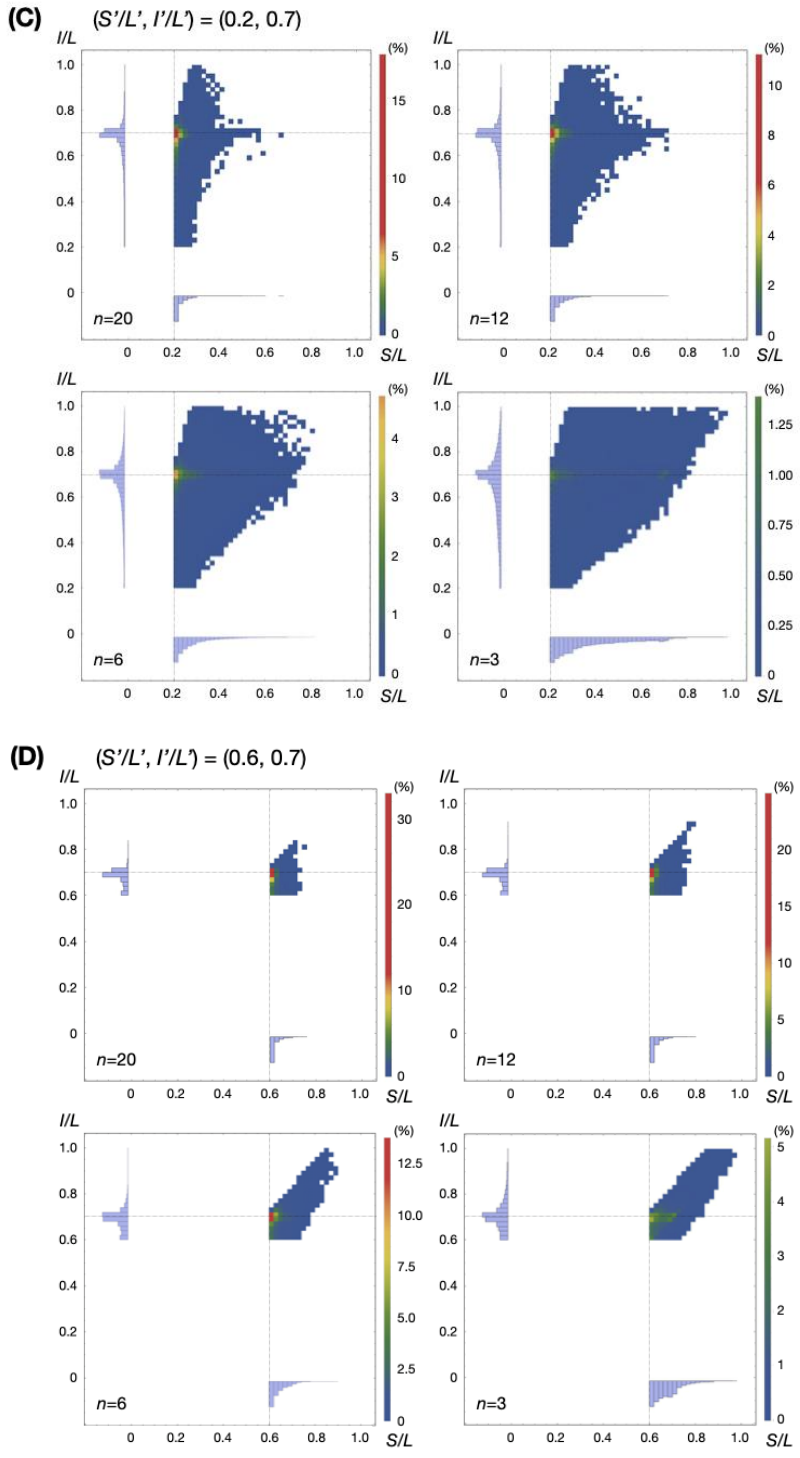

fig. S5. The frequency distributions of form parameters (*S*/*L*, *I*/*L*) evaluated for a rotating ellipsoid with different semimajor axis ratios (*S'*/*L'*, *I'*/*L'*). The individual frequency distributions of *S*/*L* and *I*/*L* are also shown as histograms. (**A**) (*S'*/*L'*, *I'*/*L'*) = (0.431, 0.641). (**B**) (*S'*/*L'*, *I'*/*L'*) = (0.3, 0.5). (**C**) (*S'*/*L'*, *I'*/*L'*) = (0.2, 0.7). (**D**) (*S'*/*L'*, *I'*/*L'*) = (0.6, 0.7).

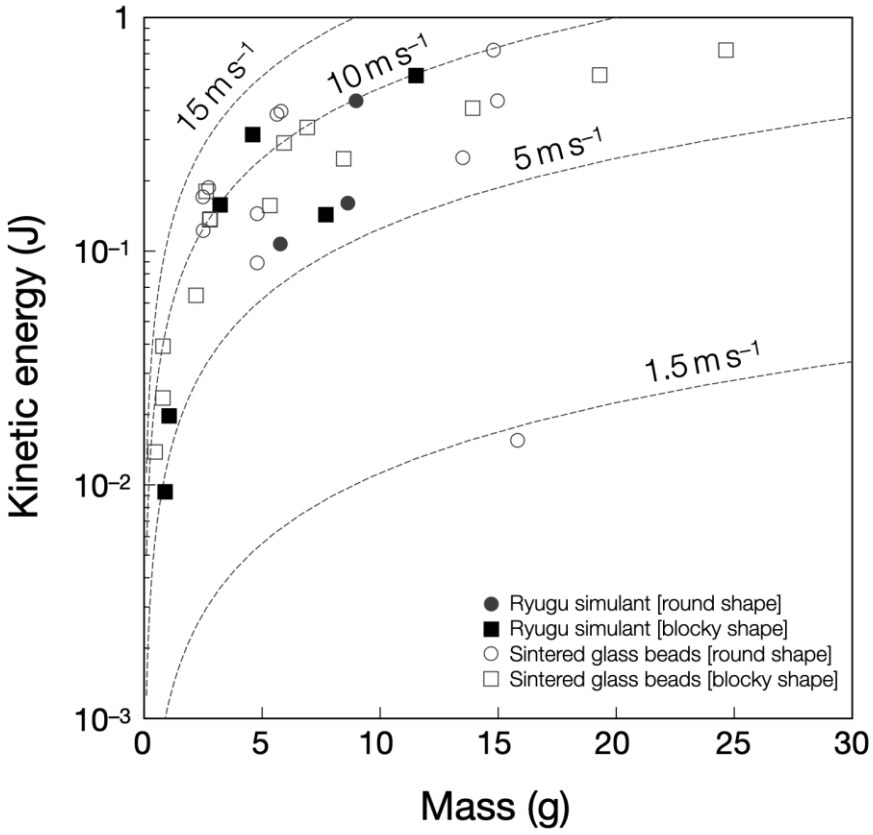

fig. S6. Impact kinetic energy required for catastrophic disruption of sintered glass beads and simplified Ryugu simulants as a function of target's mass. The impact-velocity contours are also shown.

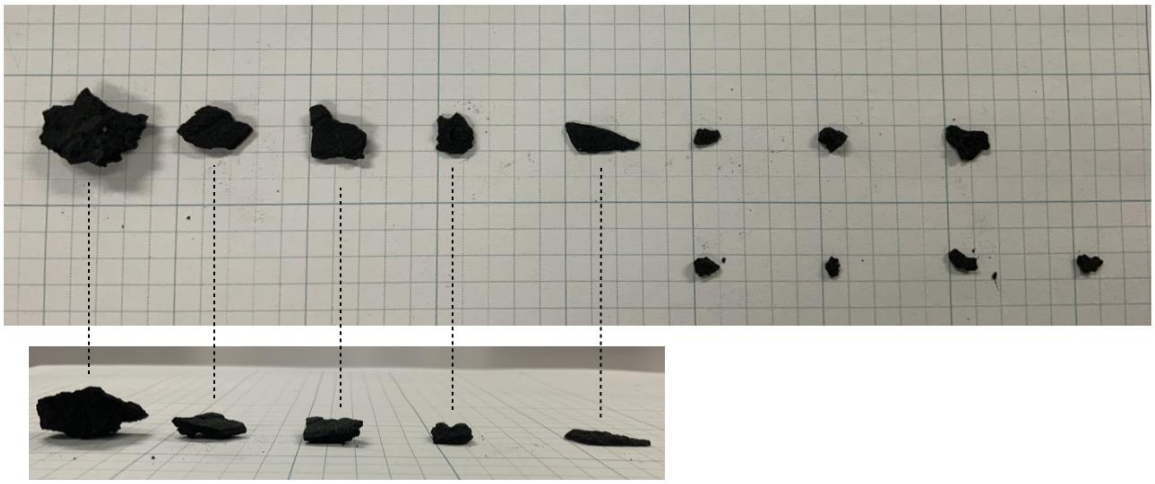

fig. S7. Impact ejecta pebbles formed through destruction of a 15 cm-sized Ryugu simulant. The background mesh size is 5 mm.

Table S1. Shape properties of particles observed by CAM-H during the TD1 operation.

Particle	Number of images	*L* (pix)	*I* (pix)	*S* (pix)	*S/L*	*I/L*	Solidity (2σ)
1-65	28	36.6	23.7	21.3	0.58	0.65	0.85 (0.07)
1-29	25	50.2	24.8	15.4	0.31	0.49	0.77 (0.16)
1-76	25	21.8	11.8	7.2	0.33	0.54	0.84 (0.13)
1-66	20	18.7	9.8	6.6	0.35	0.52	0.83 (0.07)
1-49	20	21.2	15.0	7.8	0.37	0.71	0.84 (0.09)
1-80	20	13.0	8.4	7.8	0.60	0.65	0.85 (0.08)
1-78	19	13.0	10.0	4.9	0.38	0.77	0.85 (0.07)
1-79	18	23.3	10.5	6.6	0.28	0.45	0.78 (0.14)
1-74	15	15.3	7.0	5.0	0.33	0.46	0.87 (0.08)
1-81	15	14.9	7.5	6.0	0.40	0.51	0.85 (0.10)
1-72	14	17.2	6.1	5.0	0.29	0.35	0.81 (0.15)
1-07	14	20.0	13.7	11.7	0.59	0.69	0.87 (0.10)
1-04	13	17.2	11.6	8.9	0.52	0.67	0.83 (0.08)
1-77	13	17.8	13.0	12.7	0.71	0.73	0.91 (0.04)
1-02	12	18.4	13.9	9.8	0.53	0.76	0.82 (0.14)
1-46	11	16.8	9.0	5.0	0.30	0.54	0.83 (0.07)
1-82	11	17.8	11.5	7.6	0.43	0.65	0.85 (0.08)
1-44	11	46.3	27.1	23.4	0.51	0.59	0.86 (0.15)
1-64	11	12.8	9.2	6.5	0.51	0.72	0.85 (0.10)
1-55	11	15.7	11.0	8.0	0.51	0.70	0.84 (0.09)
1-22	11	39.8	22.9	22.4	0.56	0.58	0.80 (0.19)
1-39	11	12.8	10.0	8.3	0.65	0.78	0.84 (0.13)
1-05	11	12.1	8.0	8.0	0.66	0.66	0.86 (0.10)
1-75	10	19.1	10.3	7.0	0.37	0.54	0.82 (0.13)
1-40	10	31.6	20.9	15.0	0.47	0.66	0.87 (0.09)
1-06	10	19.2	12.3	9.8	0.51	0.64	0.87 (0.05)
1-71	10	15.6	12.5	10.0	0.64	0.80	0.86 (0.04)
1-47	9	16.6	11.3	6.7	0.40	0.68	0.87 (0.09)
1-57	9	13.0	9.5	6.0	0.46	0.73	0.86 (0.05)
1-48	9	12.7	8.5	6.0	0.47	0.67	0.87 (0.08)
1-50	8	16.1	9.2	5.0	0.31	0.57	0.80 (0.15)
1-51	8	18.4	10.8	8.9	0.48	0.58	0.83 (0.12)
1-43	8	29.1	16.2	15.1	0.52	0.56	0.80 (0.07)
1-59	8	15.0	12.0	8.0	0.53	0.80	0.85 (0.15)
1-70	8	28.1	16.8	15.2	0.54	0.60	0.88 (0.04)
1-12	8	16.8	11.2	9.4	0.56	0.67	0.84 (0.11)
1-61	8	27.7	21.9	19.6	0.71	0.79	0.84 (0.08)
1-62	7	18.9	9.1	7.0	0.37	0.48	0.83 (0.12)
1-30	7	34.4	17.5	14.2	0.41	0.51	0.79 (0.14)
1-60	7	19.2	13.3	9.8	0.51	0.69	0.87 (0.12)
1-13	7	15.8	11.3	8.4	0.53	0.72	0.85 (0.13)
1-52	7	18.6	11.3	10.0	0.54	0.61	0.83 (0.12)
1-16	7	28.0	15.8	16.0	0.57	0.56	0.88 (0.07)
1-54	7	11.7	10.0	8.0	0.69	0.86	0.88 (0.05)
1-09	6	16.6	11.0	6.8	0.41	0.66	0.86 (0.09)
1-73	5	28.6	14.8	11.2	0.39	0.52	0.85 (0.05)
1-03	5	14.8	11.6	8.0	0.54	0.79	0.87 (0.08)
1-19	5	14.8	11.0	9.0	0.61	0.75	0.88 (0.05)

1-31	5	14.3	11.3	9.0	0.63	0.79	0.86 (0.11)
1-69	5	12.1	10.0	8.1	0.67	0.83	0.89 (0.07)
1-53	5	12.8	9.8	8.9	0.69	0.76	0.84 (0.05)
1-17	4	46.5	25.6	20.8	0.45	0.55	0.81 (0.12)
1-58	4	23.4	12.0	10.5	0.45	0.51	0.84 (0.10)
1-68	4	12.8	7.4	7.6	0.59	0.58	0.85 (0.12)
1-56	3	13.6	7.1	5.0	0.37	0.52	0.89 (0.11)
1-38	3	22.1	12.0	9.1	0.41	0.54	0.80 (0.09)
1-67	3	18.4	13.6	9.4	0.51	0.74	0.83 (0.06)
1-83	3	17.2	10.5	9.4	0.55	0.61	0.87 (0.01)
1-10	3	12.2	7.0	7.8	0.64	0.58	0.82 (0.12)
1-41	2	18.0	9.9	8.0	0.44	0.55	0.82 (0.12)
1-42	2	12.8	8.0	6.9	0.54	0.62	0.87 (0.09)
1-36	2	15.3	9.2	8.5	0.55	0.60	0.81 (0.15)
1-45	2	20.8	12.0	12.0	0.58	0.58	0.87 (0.03)

Number of images: Number of images used to evaluate the particle shape.
L, *I*, *S*: Form dimensions (*23*). *L* and *I* are the longest and shortest caliper dimensions measured on the maximum-area projection, and *S* is the shortest caliper dimension measured on the minimum-area projection.
Solidity: The area of a shape divided by the area of its convex hull. The average of the solidity obtained for each projection is listed with its 2-sigma standard deviation.

Table S2. Shape properties of particles observed by CAM-H during the TD2 operation.

Particle	Number of images	*L* (pix)	*I* (pix)	*S* (pix)	*S/L*	*I/L*	Solidity (2σ)
2-19	46	12.1	6.0	5.0	0.41	0.50	0.87 (0.08)
2-29	36	10.0	7.0	5.5	0.55	0.70	0.84 (0.12)
2-20	31	13.0	5.9	4.0	0.31	0.46	0.83 (0.10)
2-04	22	14.8	12.0	10.7	0.73	0.81	0.87 (0.08)
2-15	18	13.6	8.5	6.1	0.45	0.62	0.87 (0.05)
2-32	18	7.6	5.0	4.0	0.53	0.66	0.88 (0.06)
2-21	17	8.6	5.8	4.0	0.47	0.68	0.88 (0.11)
2-22	15	11.2	8.0	4.0	0.36	0.72	0.88 (0.06)
2-23	13	9.8	7.0	6.0	0.61	0.71	0.89 (0.08)
2-17	12	11.7	6.0	4.0	0.34	0.51	0.86 (0.05)
2-25	12	9.4	8.0	4.0	0.42	0.85	0.90 (0.09)
2-31	12	8.9	7.8	3.0	0.34	0.87	0.87 (0.14)
2-03	11	17.2	9.7	8.0	0.46	0.56	0.85 (0.07)
2-09	11	13.0	8.5	8.0	0.61	0.65	0.88 (0.06)
2-10	10	15.0	10.1	3.0	0.20	0.67	0.84 (0.11)
2-26	10	7.8	6.0	5.0	0.63	0.77	0.89 (0.07)
2-07	8	15.6	10.9	9.7	0.62	0.69	0.89 (0.14)
2-27	8	7.8	5.0	4.0	0.51	0.64	0.88 (0.11)
2-05	7	22.5	8.6	9.0	0.40	0.38	0.86 (0.06)
2-30	7	12.8	5.7	4.0	0.31	0.44	0.83 (0.14)
2-08	6	19.0	8.0	8.0	0.42	0.42	0.89 (0.06)
2-28	6	11.4	7.0	6.9	0.61	0.61	0.88 (0.04)
2-01	5	21.8	12.7	9.9	0.46	0.58	0.84 (0.06)
2-16	5	13.0	8.5	6.9	0.53	0.65	0.87 (0.07)
2-02	4	25.2	17.4	14.3	0.57	0.69	0.90 (0.04)
2-12	4	10.0	8.7	7.0	0.70	0.87	0.84 (0.07)
2-24	4	8.6	6.0	6.0	0.70	0.70	0.89 (0.10)
2-11	3	27.8	17.5	16.0	0.58	0.63	0.82 (0.10)
2-13	3	16.6	11.9	9.4	0.56	0.71	0.83 (0.07)
2-14	3	16.8	8.4	8.9	0.53	0.50	0.85 (0.06)
2-18	3	14.3	11.0	8.0	0.56	0.77	0.89 (0.03)
2-33	3	7.2	4.7	3.0	0.42	0.65	0.86 (0.20)
2-34	2	10.3	6.0	6.0	0.58	0.58	0.87 (0.15)

Number of images: Number of images used to evaluate the particle shape.
L, *I*, *S*: Form dimensions (*23*). *L* and *I* are the longest and shortest caliper dimensions measured on the maximum-area projection, and *S* is the shortest caliper dimension measured on the minimum-area projection.
Solidity: The area of a shape divided by the area of its convex hull. The average of the solidity obtained for each projection is listed with its 2-sigma standard deviation.

Table S3. Size and shape properties of particles in the sample catcher.

Particle	Maximum caliper length (mm)		Minimum caliper length (mm)		Height (mm)		*I*/*L*		*S*/*L*	
Chamber A										
A0008	3.858	± 0.006	2.670	± 0.006	2.51	± 0.21	0.692	± 0.002	0.650	± 0.054
A0019	3.534	± 0.006	3.060	± 0.006	1.50	± 0.32	0.866	± 0.002	0.423	± 0.091
A0046	3.781	± 0.012	2.743	± 0.012	2.35	± 0.32	0.725	± 0.004	0.622	± 0.085
A0048	3.734	± 0.008	1.651	± 0.008	1.24	± 0.21	0.442	± 0.002	0.332	± 0.056
A0069	2.654	± 0.004	1.679	± 0.004	1.24	± 0.21	0.633	± 0.002	0.466	± 0.079
A0083	1.724	± 0.004	1.275	± 0.004	0.91	± 0.21	0.740	± 0.003	0.530	± 0.122
Chamber C										
C0002	8.648	± 0.012	4.814	± 0.012	3.28	± 0.65	0.557	± 0.002	0.380	± 0.075
C0004	5.692	± 0.006	4.684	± 0.006	2.39	± 0.32	0.823	± 0.001	0.420	± 0.056
C0013	3.196	± 0.006	2.235	± 0.006	1.60	± 0.32	0.699	± 0.002	0.499	± 0.100
C0019	2.647	± 0.006	2.159	± 0.006	1.88	± 0.32	0.816	± 0.003	0.712	± 0.121
C0028	2.365	± 0.004	0.927	± 0.004	1.13	± 0.21	0.477	± 0.002	0.392	± 0.089
C0055	2.075	± 0.004	0.728	± 0.004	1.02	± 0.21	0.493	± 0.002	0.351	± 0.101

Maximum caliper length: The longest caliper length of the particle projection.
Minimum caliper length: The shortest caliper length of the particle projection.
Height: The height of the particle from the bottom of the sapphire glass dish
L, *I*, *S*: Among the caliper lengths of the projection and the height, the longest dimension is assigned as *L*, the second longest dimension as *I*, and the shortest dimension as *S*.

Movie S1.
Animation of TD1 operation synthesized from time sequence images taken by CAM-H.

Movie S2.
Animation of TD2 operation synthesized from time sequence images taken by CAM-H.

Movie S3.
Animation created from ONC-W1 time sequence images obtained with a time interval of 2 seconds during the TD2 operation. The animation was created from the ONC-W1 Level 2C images (distortion-corrected radiance data). The lower and upper limits of pixel values in each image are set to 0.0 and 1.7 W m^{-2} sr^{-1}, respectively.

Movie S4.
The demonstration movie capture of the Ta-projectile shooting to the surface target made of Ryugu simulants (*35*) on December 28, 2018. The capture was taken at a frame rate of 420 images per second but is played at about 14 times longer than the actual time.